JACS
JOURNAL OF THE AMERICAN CHEMICAL SOCIETY
pubs.acs.org/JACS
Article

Structure–Spectroscopy Correlations for Intermediate Q of Soluble Methane Monooxygenase: Insights from QM/MM Calculations

Christine E. Schulz, Rebeca G. Castillo, Dimitrios A. Pantazis, Serena DeBeer,* and Frank Neese*

Cite This: J. Am. Chem. Soc. 2021, 143, 6560–6577

ABSTRACT: The determination of the diiron core intermediate structures involved in the catalytic cycle of soluble methane monooxygenase (sMMO), the enzyme that selectively catalyzes the conversion of methane to methanol, has been a subject of intense interest within the bioinorganic scientific community. Particularly, the specific geometry and electronic structure of the intermediate that precedes methane binding, known as intermediate Q (or $MMOH_Q$), has been debated for over 30 years. Some reported studies support a bis-μ-oxo-bridged $Fe(IV)_2O_2$ closed-core conformation $Fe(IV)_2O_2$ core, whereas others favor an open-core geometry, with a longer Fe–Fe distance. The lack of consensus calls for a thorough re-examination and reinterpretation of the spectroscopic data available on the $MMOH_Q$ intermediate. Herein, we report extensive simulations based on a hybrid quantum mechanics/molecular mechanics approach (QM/MM) approach that takes into account the complete enzyme to explore possible conformations for intermediates $MMOH_{ox}$ and $MMOH_Q$ of the sMMOH catalytic cycle. High-level quantum chemical approaches are used to correlate specific structural motifs with geometric parameters for comparison with crystallographic and EXAFS data, as well as with spectroscopic data from Mössbauer spectroscopy, Fe K-edge high-energy resolution X-ray absorption spectroscopy (HERFD XAS), and resonance Raman $^{16}O-^{18}O$ difference spectroscopy. The results provide strong support for an open-core-type configuration in $MMOH_Q$, with the most likely topology involving mono-oxo-bridged Fe ions and alternate terminal Fe-oxo and Fe-hydroxo groups that interact via intramolecular hydrogen bonding. The implications of an open-core intermediate Q on the reaction mechanism of sMMO are discussed.

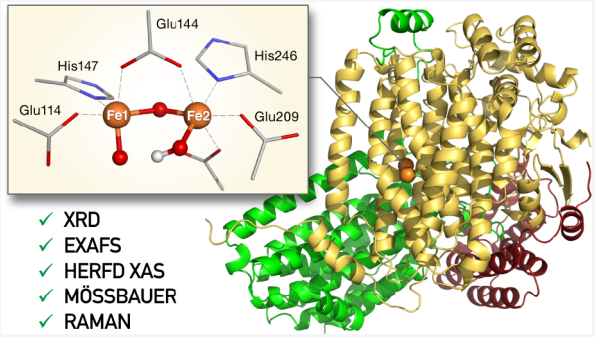

1. INTRODUCTION

In nature, methane is oxidized to methanol under ambient temperature and pressure by methane monooxygenases (MMOs) in methanotrophic bacteria via O_2 activation.[1−3] These enzymes can be categorized into two main classes: particulate MMO (pMMO) that contains a copper active site and the iron-containing soluble MMO (sMMO), which is expressed in the absence of copper.[4−9] The sMMO enzyme consists of four protein units: the hydroxylase (MMOH), which contains the diiron active site, a regulatory protein (MMOB), which facilitates substrate access to the active site, and a reductase (MMOR) and the auxiliary protein MMOD, which is thought to inhibit MMOH.[10,11] MMOH itself consists of an $\alpha\beta\gamma$ motif as shown in Figure 1. The diiron active site is located close to the MMOH surface, to which it is connected by a channel, leading to a cavity at the active site.[12,13] The active site in MMOH contains two iron ions bridged by glutamate and solvent-derived oxygen ligands.[14] In the diferric resting state ($MMOH_{ox}$),[15] the two high-spin irons are antiferromagnetically coupled, leading to a spin singlet ground state. Upon two-electron reduction provided by NADH-reduced MMOR, the diferrous state ($MMOH_{red}$) is able to react with dioxygen, yielding a peroxo intermediate ($MMOH_p$). After breaking of the O–O bond, the intermediate $MMOH_Q$ is formed. This is the key intermediate in the catalytic cycle that carries out methane activation and has thus been the subject of extensive experimental and theoretical studies.[8,14,16−28]

$MMOH_Q$ was first observed in 1993 by UV–vis absorption spectroscopy.[25] Mössbauer spectroscopy revealed that it consists of two antiferromagnetically coupled Fe(IV) ions.[26] Although there is no crystal structure of $MMOH_Q$, the extended X-ray absorption fine structure (EXAFS) data were interpreted in terms of an unusually short Fe–Fe distance of 2.46 Å in connection with two short Fe–O bonds to each iron.[22] Resonance Raman experiments, in conjunction with isotope labeled oxygen, showed that both oxygen atoms of the O_2 molecule are incorporated in $MMOH_Q$.[17] Combining this

Received: January 31, 2021
Published: April 22, 2021

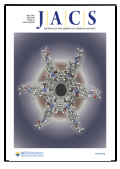

https://doi.org/10.1021/jacs.1c01180
J. Am. Chem. Soc. 2021, 143, 6560–6577

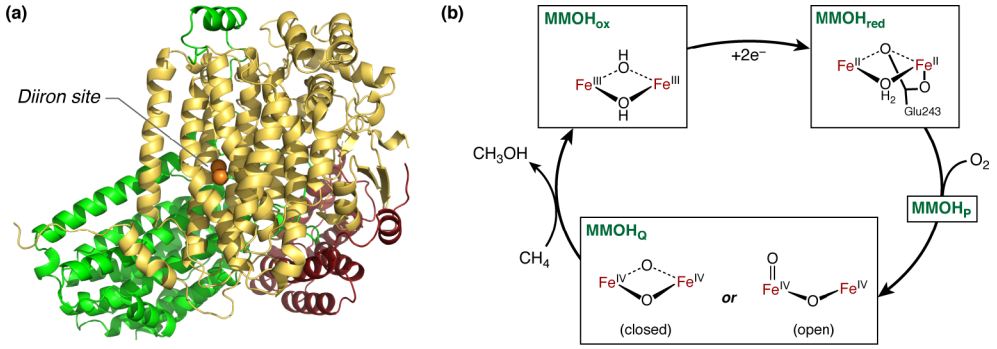

Figure 1. (a) Structural overview of the MMOH protein, and its three subunits (α, yellow; β, green; γ, red), with the α subunit harboring the diiron site. (b) Abbreviated reaction cycle of MMOH, featuring the resting state $MMOH_{ox}$, $MMOH_{red}$, and the $MMOH_Q$ intermediate. Note that for $MMOH_{ox}$ the protonation states of the μ-oxo bridges are not unambiguously resolved.

information led to the notion that $MMOH_Q$ contains a closed bis-μ-oxo ("diamond") Fe_2O_2 core (Figure 1b). Although $MMOH_Q$ has inspired numerous synthetic model complexes,[29−32] the proposed geometry with a short Fe−Fe distance has not been reproduced by any synthetic models.[20,32,33] Recent high energy resolution fluorescence detected (HERFD) EXAFS studies of $MMOH_Q$ revisited the older assignments and corrected the Fe−Fe distance to a much longer separation of ∼3.4 Å,[28] which supports other geometries, commonly referred to as open-core conformations (Figure 1b). Further, even if indirect, support for open cores comes from synthetic model complexes, which are more active toward C−H bond activation than those containing closed Fe_2O_2 cores.[34] Moreover, Fe K-edge HERFD-XAS studies showed that the pre-edge region in $MMOH_Q$ does not match with the pre-edge of the Fe(IV)Fe(IV) close core model complex, but it is rather similar to the open-core model complex pre-edges.[27] In the same study, TDDFT calculations were used to rationalize the XAS spectra, providing confidence to the assignments and to the methodological approach.

The new experimental results on $MMOH_Q$ urge for a careful and thorough revision of past spectroscopic interpretations, and the development of new structural models that can accommodate the current data. This can be achieved through the development of computational models that correctly connect structural features of $MMOH_Q$ with the currently known spectroscopic observables. Computational studies of this system have a long history in assisting experimental interpretation and suggesting a possible mechanism.[19,21,23,35−69] Aside from structure predictions,[19,36,37,40,41,60] both the transition from $MMOH_P$ to $MMOH_Q$[21,38,39,42,43,45,52,68] and the substrate oxidation[35,38,44,46−51,53,54,56−59,61−65,67,69] have been studied. However, most studies have been typically limited by the lack of extensive connections to spectroscopic data, in part because this information was not available at the time they were conducted. These limitations include the use of very small quantum mechanical (QM) cluster models, without including a realistic ligand set and without consideration of protein-derived structural constraints in early computational studies. In contrast, studies that attempted to incorporate the effect of the environment in a quantum mechanics/molecular mechanics approach (QM/MM) concentrated on intermediates in dioxygen[21] or methane[67] activation or comparison to other diiron enzymes.[57]

Importantly, it appears that past computational investigations of the nature of $MMOH_Q$ and of possible reaction mechanisms have been largely based on models that are no longer consistent with the most up-to-date experimental data. The incomplete account of the protein environment in most past studies, as well as the wealth of new information on the electronic and geometric structure of $MMOH_Q$, necessitates a thorough reappraisal of both the modeling approach and the structure−spectroscopy correlations themselves. Herein, we revisit the questions on the structure and properties of $MMOH_Q$ from the ground up based on a QM/MM approach that is ensured to be converged with respect to the effect of the protein and with emphasis on utilizing the available sources of spectroscopic data (including EXAFS, Mössbauer spectroscopy, X-ray absorption, and resonance Raman spectroscopies) in the theoretical evaluation of new models. First, we study the resting state $MMOH_{ox}$ and then we focus on a wide variety of models to describe $MMOH_Q$, examining how their geometric features and protonation states correlate with the complete range of spectroscopic properties currently available on the system. Our results enable us to narrow down the possible formulations of $MMOH_Q$ and to propose revised schemes for the conceivable reaction mechanisms of sMMO.

2. MODELS AND METHODS

2.1. Structural Analysis of XRD Models. The first step in building a computational model of the MMOH diiron active site (Figure 2) is an analysis of the existing structural data from crystallography. Structural information about $MMOH_{ox}$ can be obtained using XRD or EXAFS Spectroscopy.[2,14,22,28,70] In total, 28 individual structures of MMOH are available in the RCSB.[12,14,71−74] Yet, all of these were obtained under different conditions because the maturation of MMOH was studied using various apo-structures.[72] Structures of the maturated MMOH are available in both resting and

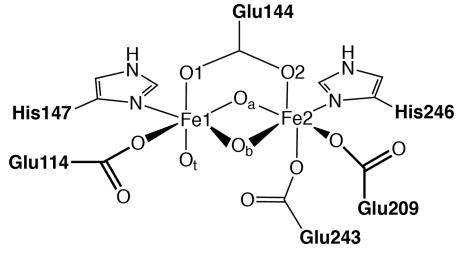

Figure 2. Schematic representation of the diironactive site including the first ligand sphere: O_t denotes the terminal oxygen, O_a is pointing toward the histidines, and O_b is directed toward the water-containing cavity that leads to the surface of the protein. In $MMOH_{ox}$, the protonation states for these oxygens are unknown.

https://doi.org/10.1021/jacs.1c01180
J. Am. Chem. Soc. 2021, 143, 6560−6577

reduced states: $MMOH_{ox}$[14,71] and $MMOH_{red}$.[73] Starting from these, large studies were done on pH dependence[73] or the effect of alcohols or alcoholates as bridging ligands to the irons.[74] Most recently, a structure of the MMOH+MMOB complex was resolved.[13,75] However, not all of these crystal structures (Table S1) contain an intact Fe_2O_2 unit. For this reason, we have performed a careful analysis and selection of crystallographic data, as described in the Supporting Information and presented in Table S2.

The results of this analysis with respect to the distribution of Fe−Fe and Fe−O distances in presumably intact XRD models are presented in Figure 3 and discussed in the Supporting Information. If

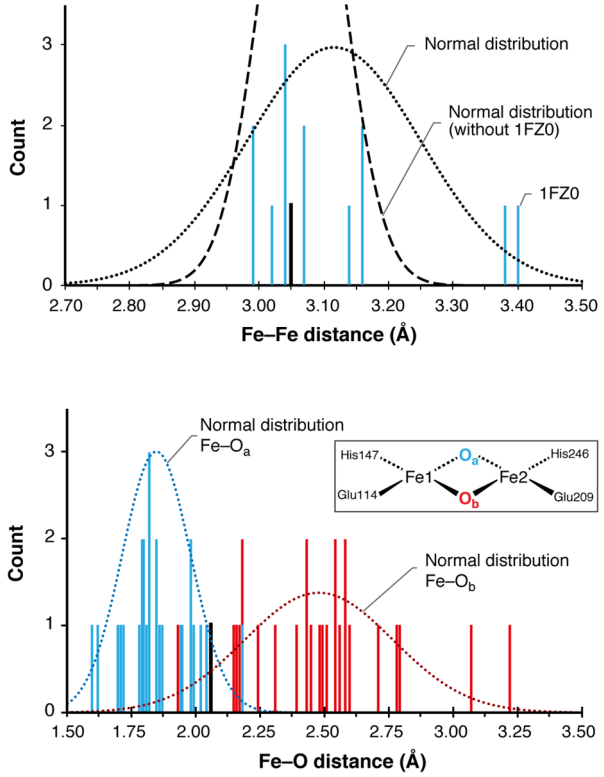

Figure 3. Analysis of Fe−Fe and Fe−O distances of nine intact $MMOH_{ox}$ active sites. Distance count rounded to two digits. The HERFD-EXAFS scatter for the Fe−Fe distance and short Fe−O distance is shown in black.

mixed-valence outliers (1FZ0[73]) are excluded, we would reach an average Fe−Fe distance of 3.07 ± 0.06 Å, which is in excellent agreement with the HERFD-EXAFS distances of 3.06 Å[28] and previous EXAFS.[76] The mean Fe−O_a distance is 1.85 ± 0.13 Å, and the mean Fe−O_b distance is 2.41 ± 0.22 Å. Figure 3 suggests that O_a is more constrained than O_b, which adopts a wider variety of bonding positions, presumably as a result of its environment (O_b is oriented toward a water filled cavity). An important question is the compatibility between XRD and HERFD-EXAFS results. EXAFS only resolves average distances between Fe and its surrounding atoms, being typically unable to distinguish scatterers with similar atomic weight such as O and N if they are at similar distance. The shortest Fe−O/N distances were fitted to 1.96 Å[77] or 2.06 Å,[28] with a resolution of 0.17 Å. Since the short Fe−O distances are expected at ca. 1.85 Å, they will overlap with Fe−O/N distances to the Glu and His ligands. HERFD-EXAFS resolves a longer Fe−O/N distance of 2.48 Å, which can be attributed to either the Fe−O_t or the longer Fe−O_b distance, in agreement with the XRD averages of 2.48 Å (Fe−O_b) and 2.31 ± 0.12 Å (Fe−O_t).

2.2. Construction of the QM/MM Model. Based on the crystal structure analysis, the 1MTY[14] crystal structure was chosen as a starting point for the QM/MM calculations. Hydrogens and water were added using the CHARMM27 force field.[78] The crystallographic water positions were maintained. In addition, a water droplet with at least 10 Å buffer around the protein was created, leading to a total of 90,000 atoms (Figure 4a). Hydrogen and water positions were

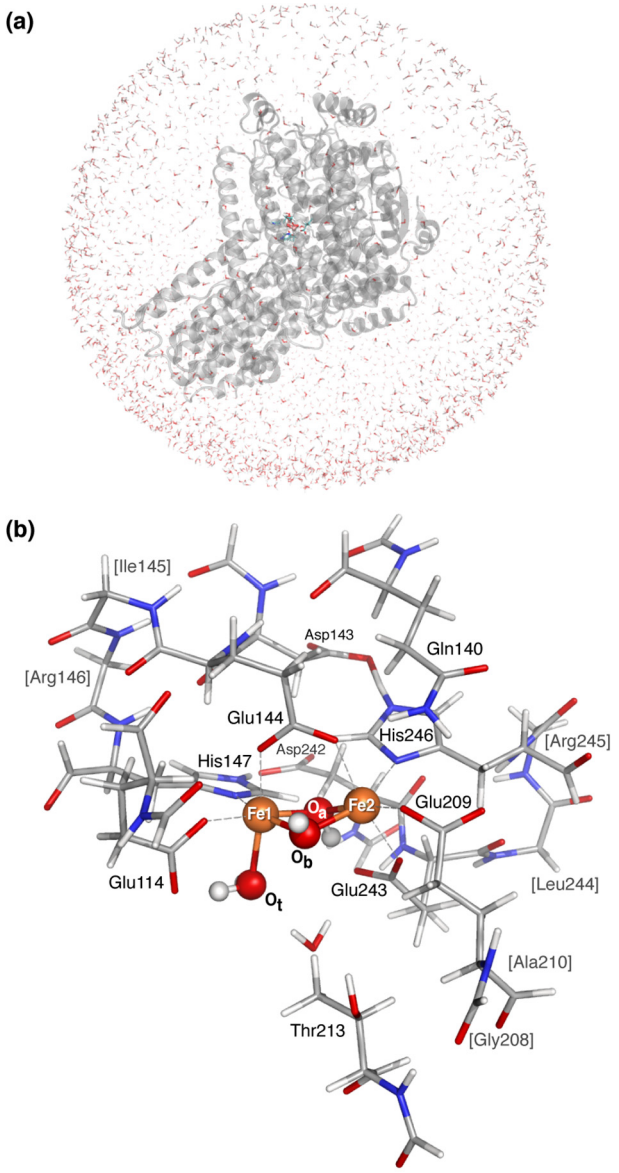

Figure 4. (a) Complete system overview of the solvated MMOH protein, (b) first and second solvation sphere around the diiron active site as used in the QM subsystem, including link atoms.

optimized for 10,000 steps before a stepwise equilibration for 50,000 steps in total. The QM region consists of the first and second layer of amino acids around the Fe_2O_x cluster, in total around 210 atoms depending on the protonation state of the bridging oxo groups (Figure 4b). Since the putative bis-μ-oxo structure of $MMOH_Q$ is remotely similar to the core geometry of $MMOH_{ox}$, the same structure was used as a starting point for the geometry optimizations for the $MMOH_Q$ models. Only models with bridging Glu243 ligands required more flexibility in the backbone of the glutamate, than the 1MTY structure could accommodate. Hence, here the hydroxylase part of the 4GAM crystal structure[12] was used as a starting point. Note that due to the limited resolution of 2.9 Å and the bridging Glu243 in the $MMOH_{ox}$ state, the 4GAM structure was not considered a fitting starting point for $MMOH_{ox}$ models. The MM structure was prepared analogous to the 1MTY structure, with a total

https://doi.org/10.1021/jacs.1c01180
J. Am. Chem. Soc. 2021, 143, 6560−6577

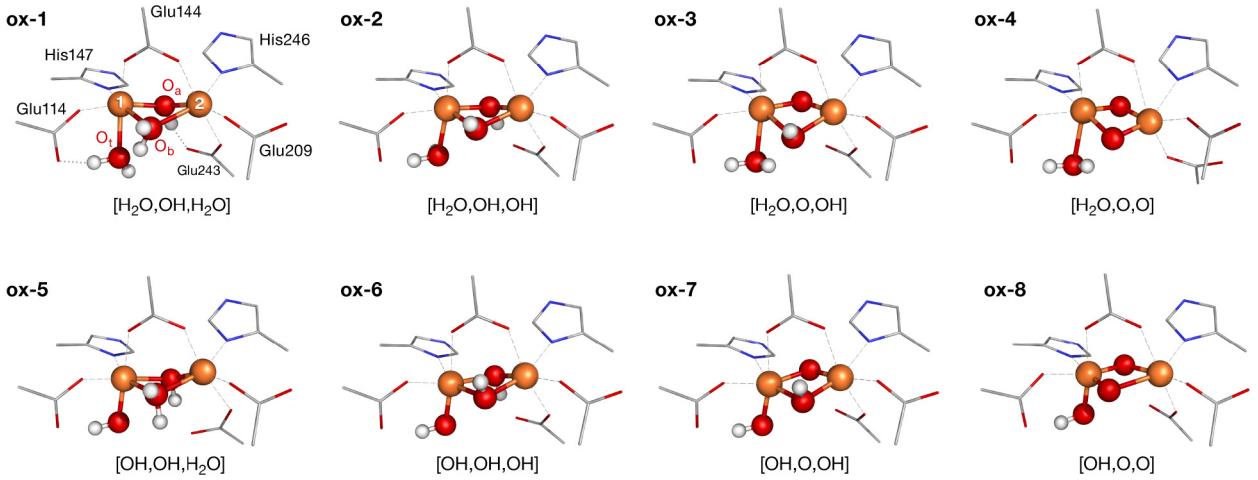

Figure 5. Geometries of the Fe_2O_x core from optimized $MMOH_{ox}$ structures. A schematic representation of the $MMOH_{ox}$ core structures is provided in Figure S4.

system size of 90,000 atoms. For the QM models, the analogous residues were chosen, so that the number of QM atoms derived from both crystal structures is the same.

2.3. Computational Details. All calculations were performed with the ORCA program package.[79,80] QM/MM calculations used an interface of ORCA with NAMD.[81−83] Geometries were optimized in the high-spin state following the same protocol as ref 27 using the BP86 functional,[84,85] with def2-TZVP basis sets[86] on Fe, N, and O, while def2-SVP basis sets were used for C and H. The RI-J approximation was used with def2/J basis sets. For the optimizations, TightOpt settings with tighter integration grids (Grid6) were used. Dispersion corrections were included using D3BJ.[87] Mössbauer parameters were calculated according to ref 88 using the B3LYP functional[89,90] with core-property CP(PPP)[91] basis sets. For the Fe atoms, tighter grids and integration accuracy (SpecialGridIntAcc 7) were used. Mössbauer spectra were simulated using the "mf" program written by Dr. E. Bill.[92] X-ray absorption spectra were calculated using TD-DFT,[93,94] again with the B3LYP functional with a def2-TZVP basis. Spectra were plotted with an applied broadening of 1.0 eV using the orca_mapspc utility. An energy shift of 150.85 eV was applied, as determined by the difference between calculated XAS spectra and experimental HERFD XAS pre-edge energies for model complexes.[27] We note that due to the relatively limited HERFD XAS data that are available, a smaller calibration set (Figure S1) was utilized as compared to previous TFY/transmission XAS calibration studies.[95,96] A graphical summary of the experimental vs calculated energy shift is given in Figure S2. It should be noted that the exact shift depends on the chosen methodology.[96] Similarly, the scaling factor for the calculated vs experimental areas can be obtained as shown in Figure S3. The scaling factor depends on how exactly the calculated area is determined. Here, the area was determined by calculating the sum of the oscillator strengths. Arguably the quality of the extrapolation increases with the number of data points, therefore the pre-edges were separated into individual peaks. Following this analysis, the pre-edge areas are scaled by a factor of 5.97. Nonresonant Raman spectra were calculated using the same level of theory as the geometry optimizations. Isotope labeled Raman spectra were obtained using the orca_vib program. The Raman spectra were plotted with an applied broadening of 5 cm^{-1} using the orca_plot utility.

3. RESULTS AND DISCUSSION

3.1. Models of $MMOH_{ox}$. To directly compare possible protonation states of $MMOH_{ox}$, a set of models (Figure S4) was constructed in order to test the flexibility of the system and the ability of our computational approach to differentiate between different protonation states. These models start with a terminal water and a μ-OH/μ-OH_2 bridging ligand (model **ox-1**). The bridging ligands are successively deprotonated up until model **ox-4** with a bis-μ-oxo core. Similarly, models with terminal hydroxo ligands were constructed, again with a μ-OH/μ-OH_2 bridge (model **ox-5**). These were also systematically deprotonated leading up to a bis-μ-oxo core at model **ox-8**. The geometries of the diiron cores after geometry optimization are shown in Figure 5.

3.1.1. Molecular Structure of $MMOH_{ox}$. Some general trends in the models can be deduced directly from Table 1.

Table 1. Structural Data for the Possible $MMOH_{ox}$ Structures shown in Figure 5[a]

Model	Fe_1−Fe_2	Fe_1−O_t	Fe_1−O_a	Fe_2−O_a	Fe_1−O_b	Fe_2−O_b
ox-1	3.29	2.21	1.96	1.97	2.29	2.36
ox-2	3.07	2.20	1.97	1.98	2.05	2.17
ox-3	2.95	2.25	1.85	1.85	2.19	2.08
ox-4	2.67	2.24	1.88	1.83	1.89	1.88
ox-5	3.31	1.90	2.10	1.93	2.21	2.33
ox-6	3.09	1.84	2.03	1.91	2.22	2.06
ox-7	2.92	1.88	1.92	1.78	2.15	2.03
ox-8	2.91	1.82	1.74	1.93	1.71	2.33
XRD Average	3.07	2.31	1.80	1.90	2.35	2.61

[a]All values in Å.

The models with terminal waters have a longer Fe−O_t distance than the models with terminal hydroxo ligands. Additionally, all models have an asymmetric core: the Fe−O_a distances are shorter than the Fe−O_b distances, even for models with the same protonation state in both bridges. And last, the calculated distances to O_t and O_b are shorter than the XRD average. A plausible explanation for this is that the terminal oxygen (O_t) and the frontal bridging oxygen (O_b) are pointing toward a water filled cavity, and are thus affected by hydrogen bonding to water in this cavity. Since water molecules are not resolved in the crystal structures, it can be assumed that they are not tightly locked in rigid positions. Instead, there are many possible water positions, leading to many possible hydrogen bond confirmations. This is reflected in the variety of bond lengths in the crystal structures, leading to a larger standard deviation.

A more detailed graphical comparison of the QM/MM results with the XRD analysis is presented in Figure 6. As a

https://doi.org/10.1021/jacs.1c01180
J. Am. Chem. Soc. 2021, 143, 6560−6577

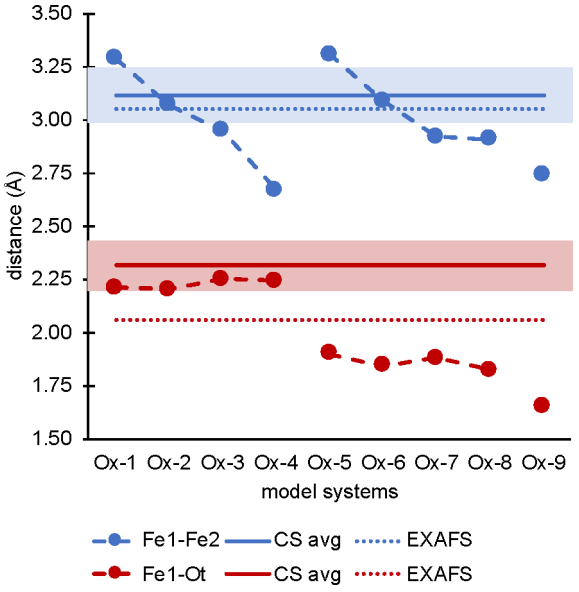

Figure 6. Graphical representation of the geometry analysis. Left: Difference of the Fe−Fe and Fe−O_t bond lengths in the models vs the crystal structure average of the 13 intact crystal structures presented in Table 1 and EXAFS distances.[28] Full lines denote the crystal structure average, dotted lines denote the EXAFS fits, and pastel bars denote the standard deviation. Note that only the shorter EXAFS Fe−O distances were included.

second level of comparison, the EXAFS distances have been included. This figure compares the difference of each distance to the corresponding crystallographic average. In doing so, the models can be ranked according to the number of distances they represent well. Additionally, the standard deviation of the crystal structures is given, to provide a trust range for each distance. Based on this comparison, models with a terminal hydroxo ligand can be excluded, since the Fe−OH distances are too short compared to the crystal structure average. Intermediate protonation states yield the best agreement for the Fe−Fe distances. The graphical comparison for the Fe−O distances is given in Figure S5, and a similar figure with the ligand distances is given in Figure S6. The Fe−O distances are best represented by models that do not feature a large spread of distances. The closest fit is achieved for models with two hydroxo bridges. Therefore, the geometric parameters of models **ox-2** and **ox-3** agree best with the available experimental data.

3.1.2. Electronic Structure of $MMOH_{ox}$. The basis for the property calculations is the electronic structure of $MMOH_{ox}$. Both irons were treated as high spin irons (local M_S = 5/2), coupled antiferromagnetically. This is achieved by first calculating the high-spin state (M_s = 5) and then flipping the spin on one iron-center followed by reconverging the self-consistent field equations to the broken-symmetry solution with M_S = 0. The correct broken-symmetry state is confirmed by inspection of the atomic spin populations and corresponding orbitals. The presence of five mostly metal-centered singly occupied orbitals on each site was confirmed, by inspection of the Mulliken spin populations (Table S3). Antiferromagnetic coupling is observed for all models except model **ox-4**, which is very weakly ferromagnetically coupled. For the $MMOH_{ox}$ models with a terminal water ligand (**ox-1** to **ox-4**), less than 5% of the spin population is found on the oxygen bridges, independent of protonation state of the bridging ligand. For models with a terminal hydroxo ligand (**ox-5** to **ox-8**), the spin population on the bridging oxygens has increased to 10−25%, and has significantly increased on the terminal oxygen (∼17−38%), which in some cases may be considered to develop partial radical character. However, there is no clear correlation of these values to the exchange coupling constant. As a representative example, the corresponding orbitals and overlap integrals of model **ox-3** are shown in Figure S7.

3.1.3. Mössbauer Parameters of $MMOH_{ox}$. In the next step, models can be evaluated using their spectroscopic properties, beginning with the Mössbauer parameters. The calculation of Mössbauer parameters focuses on the isomer shift, which is proportional to the charge density at the nucleus, and the quadrupole splitting, derived from the electric field gradient at the iron nucleus.[91] After proper calibration of the isomer shift,[88] the predicted isomer shifts tend to be more reliable than the calculated quadrupole splittings.[97,98] Thus, for more complicated iron systems, the analysis usually focuses on the isomer shift.[99] An overview on the calculated and experimental Mössbauer parameter for $MMOH_{ox}$ is given in Table 2. The

Table 2. Calculated Mössbauer Parameters for the Models Presented in Figure 5, Compared to Experimental Mössbauer Data for the $MMOH_{ox}$ Main Component[a]

	ΔE_q		δ	
Model	Fe_1	Fe_2	Fe_1	Fe_2
ox-1	−1.67	−0.95	0.49	0.44
ox-2	−1.64	0.87	0.51	0.47
ox-3	−2.09	−1.54	0.51	0.50
ox-4	2.07	1.38	0.49	0.51
ox-5	−1.52	−1.18	0.49	0.45
ox-6	−1.79	−1.32	0.50	0.48
ox-7	−2.51	−1.44	0.51	0.48
ox-8	3.10	−0.98	0.78	0.17
Experiment				
ref 15	1.20	0.95	0.50	0.50
ref 100, pH 7	1.16	0.87	0.51	0.50
ref 100, pH 9	1.77	0.70	0.54	0.50

[a]Note that the iron labels for the experimental data are arbitrary. All values in mm/s.

experimental Mössbauer data show two ferric irons with almost identical isomer shifts.[15] The quadrupole splitting shows pH dependence.[100] Simulations of the experimental parameters and calculated Mössbauer are presented in Figures S8 and S9.

An additional level of complexity arises from the fact that there are two ways of generating the $MMOH_{ox}$ intermediate: since it is the resting state, it can either be utilized as isolated[15,100] or generated by oxidizing $MMOH_{red}$, as done in recent studies.[28] For the latter, an additional signal in the Mössbauer spectrum is observed.[101−103] One hypothesis states that these originate from antisymmetric exchange that has been observed in model complexes.[101] In single turnover studies two species for the $MMOH_{ox}$ state were found.[102] They referred to the second as $MMOH_{ox}$(sl), for the slow reacting species, which is thought to be closer to the $MMOH_{red}$ geometry.

The isomer shift of the calculated ox models are all of the same order of magnitude, with the exception of **ox-8**. Several models are within or close to the experimental difference of the two isomer shifts (Δmaxδ 0.4). The quadrupole splitting, as expected, is more sensitive and shows greater fluctuation in the different models. The simulation of the calculated Mössbauer

https://doi.org/10.1021/jacs.1c01180
J. Am. Chem. Soc. 2021, 143, 6560−6577

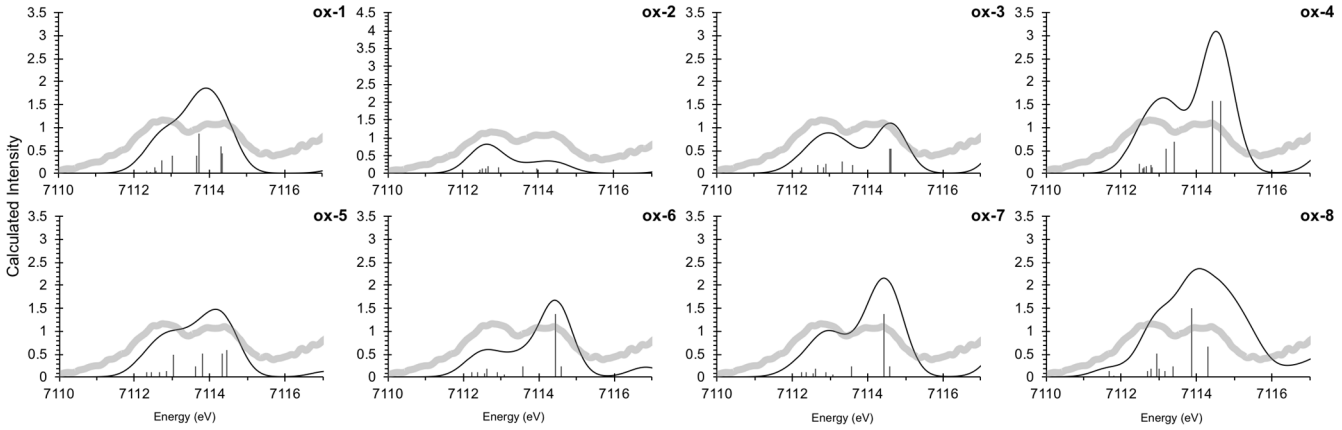

Figure 7. Calculated XAS pre-edge spectra for selected $MMOH_{ox}$ models (black) on top of the experimental spectrum (gray).[27]

Table 3. Difference between Calculated and Experimental IWAE and XAS Pre-edge Areas of the $MMOH_{ox}$ Models

model	ox-1	ox-2	ox-3	ox-4	ox-5	ox-6	ox-7	ox-8	Exp[27]
IWAE (eV)	7113.63	7113.18	7113.71	7113.91	7113.63	7113.87	7113.87	7113.8	7113.3
Area	19.62	8.03	14.28	31.97	17.78	15.95	22.85	28.20	13.37

parameters is given in Figure S9. The doublet type spectrum, as observed in earlier studies or at lower pH, is reproduced by model **ox-5**. Several models show a doublet with split tips, resulting from two irons with similar, yet distinct splittings. In models **ox-2** and **ox-7** the quadrupole splittings of the two irons are so different that two doublets are resolved. While this is reminiscent of the second species found in $MMOH_{ox}$ powder spectra,[28,101] it should be noted that the splitting of **ox-7** is larger than experimentally observed. The protonation state of the bridging oxygens might give information on the geometry of $MMOH_{ox}$(sl), but clearly further experimental investigation is needed. From the Mössbauer calculations, model **ox-8** can be safely excluded from the list of possible $MMOH_{ox}$ models. Yet, since all other models are rather close in the isomer shift, a definitive distinction based on these data alone are not possible. However, both **ox-2** and **ox-3**, which were the best models based on the geometric structure analysis, also lead to calculated Mössbauer parameters that are consistent with experiment.

3.1.4. XAS Pre-edges of $MMOH_{ox}$. X-ray absorption spectroscopy offers an additional way of evaluating the electronic structure of these models. Within a molecular orbital picture, the XAS pre-edge features correspond to transitions from the 1s metal orbital to the unoccupied 3d orbitals.[27] This leads to 10 transitions for a diferric di-iron site, leading to two peaks which, in a simple picture, can be understood as resulting from the splitting between the t_{2g} and e_g manifold of the pseudo-octahedral metal sites. The exact nature of the main transitions that give rise to this pattern have been thoroughly discussed before.[27] In model complexes,[27] it was found that equal protonation states on the μ-O bridging ligands yield a symmetric spectrum. The transitions to the t_{2g}-set (d_{xy}, d_{xz}, and d_{yz}, orbitals) comprised in the lower energy pre-edge peak show a lower intensity than the high energy pre-edge peak. The transitions overlap perfectly, indicating orbital degeneracy due to a high symmetry at the iron cores. For model complexes with asymmetric bridging ligands (μ-oxo and μ-hydroxo), the transitions do not overlap since the irons are unequal. The d_{z^2} orbitals were found to be the highest in energy and intensity, followed by the $d_{x^2-y^2}$ orbitals. The t_{2g}-set was found grouped together at lower energies, leading to a second lower energy pre-edge feature. The experimental XAS pre-edge shows two signals for $MMOH_{ox}$, separated by ~2 eV. Looking the calculated pre-edges for the protein (Figure 7), lower symmetry is expected, due to the nature of the diiron site and ligands involved. Hence, complete degeneracy would not be expected even for symmetrically protonated bridging ligands

A quantitative comparison with experiment is given in Table 3. Most models show an IWAE which is slightly larger than experiment, with the exception of **ox-2**, which is shifted to slightly lower energy. This is largely a result of the differences in the pre-edge intensity distributions. Most models reproduce the experimental shape given by two peaks, with the second calculated feature having higher intensity than the first one. Only model **ox-2** and **ox-8** deviate from this. In the case of model **ox-2**, the second pre-edge peak (~7114.4 eV) is lower in both energy and intensity; hence, the IWAE is shifted toward lower energies. Looking at the pre-edge areas, model **ox-3** is closest to the experimental area of 13.37 units, and certainly within the estimated ~10% error due to the limited data for the area regression. This is followed by **ox-6** and **ox-5**, whereas other models deviate more strongly.

3.1.5. Summary on $MMOH_{ox}$ Models. By combining the results of geometries and spectroscopy, useful conclusions regarding the structure of the $MMOH_{ox}$ intermediate can be reached. Models featuring a terminal water ligand and bridging hydroxo ligands agree best with the crystal structures. From Mössbauer spectroscopy, it can be seen that the two irons are expected to have a very similar local environment; this is achieved for **ox-5**, which features a terminal hydroxo ligand with a bridging hydroxo and water ligand. Among models with terminal water ligands, **ox-3** and **ox-4** show the best agreement, although differences among the two irons are observed. Models **ox-2** and **ox-7** will not be considered further, because they do not agree with the low-pH Mössbauer experiment. The XAS pre-edges show that although the shape and width of the calculated pre-edges are relatively consistent among models, changes in the protonation state of the bridging and terminal ligands lead to subtle differences in the distribution of

https://doi.org/10.1021/jacs.1c01180
J. Am. Chem. Soc. 2021, 143, 6560−6577

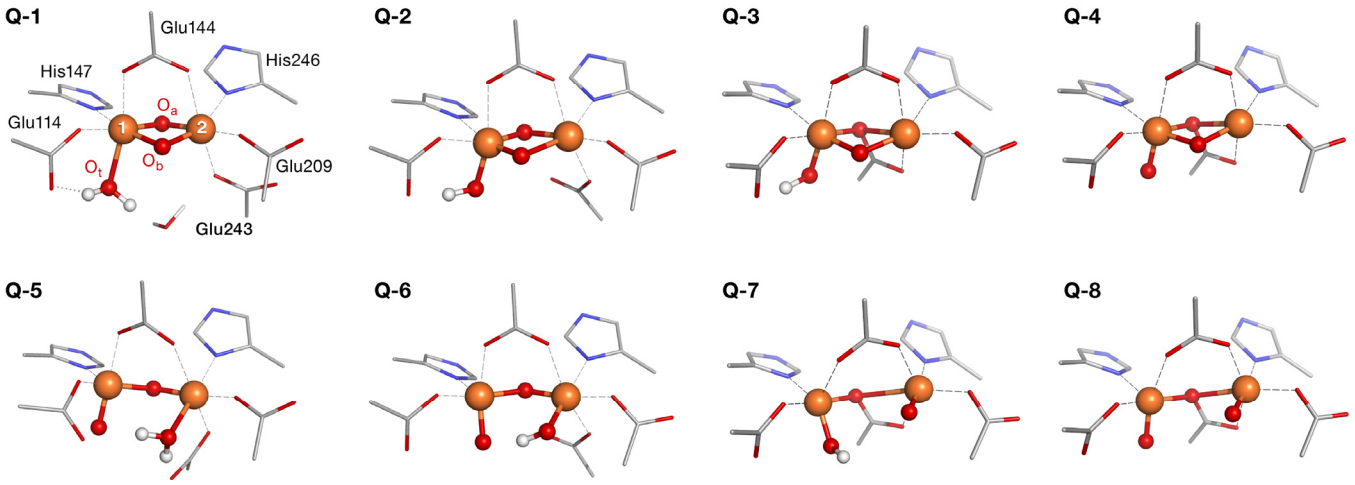

Figure 8. Optimized structures of the suggested core motifs for $MMOH_Q$. A schematic representation of the cores presented in Figure S10.

Table 4. Central Distances for the Central Iron Unit of QM/MM Optimized $MMOH_Q$ Models in Figure 8

model	Fe_1-Fe_2	Fe_1-O_a	Fe_2-O_a	Fe_1-O_b	Fe_2-O_b	Fe_2-O_t	Fe_1-O_t
Q-1	2.80	1.84	1.86	1.84	1.80	–	2.25
Q-2	2.84	1.72	2.12	1.74	1.94	–	1.78
Q-3	2.98	1.96	2.40	1.86	1.86	–	1.70
Q-4	3.03	2.04	2.34	1.83	1.90	–	1.64
Q-5	3.20	1.85	1.73	–	–	2.19	1.65
Q-6	3.21	1.72	1.86	–	–	1.66	1.80
Q-7	3.85	1.95	2.75	–	–	1.65	1.72
Q-8	3.68	1.98	2.38	–	–	1.64	1.64

intensities. The best agreement in terms of spectral shape, IWAE, and area is observed for model **ox-3**. Therefore, on average, we suggest that model **ox-3** may be considered the best candidate for $MMOH_{ox}$.

3.2. Models for $MMOH_Q$. Based on previous studies supporting closed- and open-core conformations for the key intermediate in sMMO, a set of models was constructed for the $MMOH_Q$ active site. The selection of plausible models include the following: (1) bis-μ-oxo bridged cores; (2) μ-OεGlu243 bridged diamond cores, inspired from the $MMOH_{red}$ structure, as suggested recently;[28] (3) μ-oxo bridged open cores; and (4) μ-OεGlu243 bridged open cores. A schematic representation of all models is shown in Figure S10, while Figure 8 depicts the optimized cores of eight $MMOH_Q$ models (**Q-1** to **Q-8**) chosen for further analysis. Among those models, the first four are closed cores, while the last four open up toward the cavity. While the schematic view (Figure S10) allows an easy way of classifying the models, in reality each model is only one member of a larger family of conceivable structures that differ in subtle details concerning the orientation of hydrogen bonds and the arrangement of surrounding waters. In the real system, at room temperature, there most certainly is some structure fluctuation that interconverts members of the same structural family. However, a detailed analysis of these dynamic processes is outside of the scope of this paper.

3.2.1. Molecular Structure of $MMOH_Q$. From the data presented in Table 4, it is evident that the Fe−Fe distances clearly distinguish the closed- and open-core models, with the closed cores having Fe−Fe distances between 2.8 and 3.0 Å and the open cores having distances larger than 3.2 Å. We note that these distances are all longer than the originally reported EXAFS distance of 2.46 Å,[22] but agree quite well with the respective closed- and open-core molecular models.[27] For both the closed- and open-core models the presence of the μ_1-bridging Glu243 (**Q-3**, **Q-4**, **Q-7**, and **Q-8**) results in an elongation of the Fe−Fe distance by ∼0.1 Å for the closed-core models, and more than 0.4 Å for the open-core models. Models **Q-7** and **Q-8** show an even larger Fe−Fe distance, than the HERFD EXAFS distance for the Fe−Fe vector of ∼3.4 Å.[28] Therefore, the best agreement with the experiment would be an open-core model with slightly less interaction than observed in the μ-oxo bridging models **Q-5** and **Q-6**.

The Fe−O distances within the core are more scattered than in the $MMOH_{ox}$ models. In contrast to the Fe−Fe distances, no clear pattern is observed. However, within the $MMOH_Q$ models, the Fe−O distances can be nicely grouped depending on the protonation state. $Fe-O_t$ distances to terminal oxo ligands are the shortest, between 1.64 and 1.68 Å (**Q-4** to **Q-8**). Distances to terminal hydroxo ligands are found to be 1.78 Å for closed-core models (**Q-1** and **Q-3**) and 1.79 to 1.82 Å for open-core models (**Q-6** and **Q-7**).

$MMOH_Q$ models can also be analyzed by the asymmetry of their cores. The Fe−μ-O distances in models **Q-5** and **Q-6** show an interesting pattern of asymmetry, with one short Fe−μ-O distance of 1.73 Å and a longer distance at 1.86 Å. An even more asymmetric pattern is observed in the bis-μ-oxo model **Q-2**, with a short Fe−O bond of 1.72/1.74 Å and a longer bond of 1.94/2.12 Å. In contrast, the Fe−μ-oxo distances in model **Q-1** are very symmetric, with distances between 1.80 and 1.86 Å. The longest Fe−O distances are observed for the Fe−OεGlu243 distances, in both closed- (**Q-3** and **Q-4**) and open-core models (**Q-7** and **Q-8**). Compared to the experiment (Figure 9), the averaging of the core distances in the respective model becomes important. For the

https://doi.org/10.1021/jacs.1c01180
J. Am. Chem. Soc. 2021, 143, 6560−6577

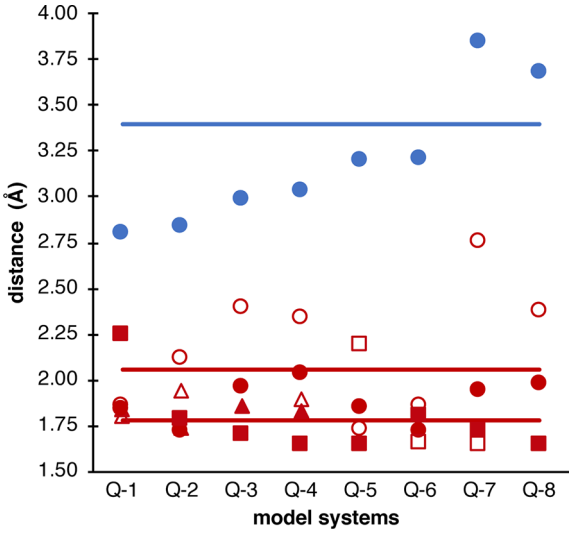

Figure 9. Graphical representation of the geometry analysis: Difference of the Fe−Fe (blue) and Fe−O bond lengths in the $MMOH_Q$ models vs the EXAFS distance. Full lines denote the EXAFS distances, with the Fe−Fe distance being estimated at 3.4 Å. The Fe−O distances are separated into Fe1 (filled) and Fe2 (empty), and O_a (circles), O_b (triangles), and O_t (squares).

sake of simplicity, the ligand distances are separately shown in Figure S11. Several models show that the core distances can be nicely averaged in a way that is consistent with the two EXAFS distances 1.78 and 2.06 Å.[28] Only model **Q-6** lacks the longer Fe−O distances in the core. However, the Fe−O/N distances to the glutamate and histidine ligands also contribute to this longer EXAFS distance. As shown in Figure S11, these agree well with the EXAFS distances.[28]

In conclusion, the geometric analysis shows that open-core models agree with the EXAFS data, while the closed cores all exhibit Fe−Fe distances that are too short. However, the Oε-Glu243 bridged open-core models **Q-7** and **Q-8** are overestimating relative to experiment. Hence the best agreement is observed for oxo bridged open-core models, like **Q-5** and **Q-6**.

3.2.2. Electronic Structure of $MMOH_Q$. The $MMOH_Q$ intermediate consists of two high-spin Fe(IV) ions which are antiferromagnetically coupled. Hence, all models were set up initially as locally high spin (M_S = 2 assumed for each Fe ion; i.e., four unpaired electrons) but in a broken symmetry state with total M_S = 0. The results were analyzed by inspection of the atomic spin populations and of the corresponding orbitals. The corresponding orbital transformation offers a convenient way of analyzing broken-symmetry wave functions by identifying the nonorthogonal valence-bond-like magnetic orbital pairs in antiferromagnetically coupled systems.[104] The procedure transforms the spin-unrestricted canonical orbitals into a set that diagonalizes their overlap matrix, i.e. each spin-up orbital has nonzero overlap with at most one spin-down orbital. The resulting orbitals are ordered according to their overlap integrals into a group of essentially doubly occupied spin-up/spin-down orbital pairs (spatial overlap close to unity), a group of unmatched magnetic orbitals where the spin-up and spin-down counterparts are localized on different sites of the molecule (spatial overlap between zero and one), and finally a set of unmatched spin-up orbitals in case the number of α electrons exceeds the number of β electrons. For a broken-symmetry M_S = 0 state of a dimer consisting of two high-spin Fe(IV) we expect four pairs of corresponding orbitals (see Figure S12 for two representative examples). These were indeed found for all models, with the exception of **Q-4**. These pairs of corresponding orbitals fall into categories of stronger coupling (overlap range of 0.7−0.8) and weaker coupling (overlap range of 0.1−0.2). In general, deviations may arise when the calculations converge to M_S = 0 solutions with locally intermediate-spin iron ions or with significant ligand radical character. The Mulliken spin populations for all models are provided in Tables S5 and S6. We observe that different models may have a different degree of spin localization, often deviating from the formal integer values expected for high-spin d^4 iron ions. Additionally, some of the models, including **Q-2** and particularly **Q-4**, have noticeable asymmetry in the two Fe ions in terms of local spin populations.

As shown in Table S5, a substantial amount of spin is found on several oxygen ligands. Especially the terminal oxo ligands show significant spin population. This is independently found in closed- (**Q-4**) and open-core models (**Q-5**−**Q-8**). The largest spin population is found on the terminal oxo ligand of **Q-4** resulting from strong spin delocalization over the Fe−O_t moiety, conferring high radical character to O_t. For the glutamate bridged models (**Q-7**, **Q-8**), almost no spin is found on the oxygen of the bridging glutamate (O_a). For μ-oxo bridged open cores (**Q-5**, **Q-6**), substantial spin is found on the bridging oxygen (O_a). An interesting comparison is between **Q-1** and **Q-2**, where in **Q-1** the spin is mostly localized on the irons, while in **Q-2** there is significant spin along the μ-oxo bridges. Inspection of the molecular orbitals confirms that in all cases the HOMO of the system has significant d_{z^2} character. Its orientation is determined by the strongest interacting σ ligand. In the case of the diiron site, the μ-oxo ligands, the glutamates, and terminal ligands (H_2O, OH, oxo) are competing. For irons with a terminal oxo ligand, the d_{z^2} orbital on that iron is oriented along the Fe−O_t bond. In the closed-core models, the d_{z^2} orbitals of the two irons are parallel, with the *xy* plane in the same plane as the μ-oxo bonds. This means that the d_{z^2} orbital is oriented along the Fe−OGlu bonds to Glu114. For the open-core models, the orientation of the d_{z^2} is determined by the orientation of the terminal oxo moiety. On the other iron, the d_{z^2} orbital is oriented along the Fe−μO bond, since this is a stronger σ ligand than the terminal H_2O or OH ligand.

Again, the QM/MM computational models can be compared to synthetic model complexes.[27,31,105] The Fe−Fe distances in the QM/MM models and the synthetic complexes agree well. The closed-core model complex and the closed-core computation models (**Q-1**, **Q-2**) show the best agreement. In the open-core models, differences are observed. In the synthetic complexes, all oxygen based ligands lie in the same plane, regardless of whether the complex is labeled as "open" or "closed". This is not the case in the open-core models in the protein and may have important implications for the comparability of the electronic structure and spectroscopic properties between the two. Here the Fe-Ot unit is perpendicular to the Fe−μO−Fe plane. The reason for this difference is the different ligand environment, from the rigid chelate ligand in the synthetic complex to the flexible oxygen-rich environment of the protein, embedded in a network of various hydrogen-bonding possibilities. As a consequence, the electronic structure and spectroscopy are not expected to be directly comparable between the QM/MM models of the enzyme and the small synthetic model complexes. Here one has to be cautious, because the model complexes feature iron

https://doi.org/10.1021/jacs.1c01180
J. Am. Chem. Soc. 2021, 143, 6560−6577

ions in an intermediate spin state (locally $M_S = 1$) and their total spin differs from the protein:[27] the closed-core model is $M_S = 0$, while the open-core model is $M_S = 2$. Therefore, no synthetic complex has a direct analogy to the natural system in terms of the electronic structure configuration of the Fe ions. In the following we focus on spectroscopic properties of the QM/MM models developed here.

3.2.3. Mössbauer Parameters of MMOH$_Q$. The Mössbauer parameters for each model are given in Table 5. As MMOH$_Q$ is a reactive intermediate, it cannot be trapped in a pure form and the raid freeze quenched sample utilized for Mössbauer experiments is comprised of at least three species (MMOH$_{red}$, MMOH$_{ox}$, and MMOH$_Q$), each with two individual irons. In modeling the experimental Mössbauer spectrum, the MMOH$_Q$ component was fit with only one parameter set for two irons, indicating that the two irons in MMOH$_Q$ can be considered equal within the resolution of obtained spectra. In the calculations, however, no symmetry constraints were used, leading to inequalities in the two Fe sites. This raises the question, by how much the parameters for each iron can differ, to still result in a two line Mössbauer spectrum, as opposed to a four line spectrum that would be obtained for highly inequivalent irons. To answer this question, the calculated spectra were simulated. Since the determination of quadrupole splitting using DFT is less reliable than the isomer shift,[106] the comparison here focuses on the isomer shift and the average of the experimental quadrupole splitting were used in the simulation (see Figure S13). The resulting simulations were compared to the simulations using the experimental parameter set (Figure 10).

Table 5. Calculated Mössbauer Parameters for the QM/MM Models Presented in Figure 9[a]

	ΔE_q		δ	
	Fe_1	Fe_2	Fe_1	Fe_2
Q-1	0.93	−0.78	0.38	0.37
Q-2	2.45	−0.58	0.65	−0.13
Q-3	−1.83	1.54	0.43	0.10
Q-4	2.22	−2.22	0.54	0.00
Q-5	−1.54	0.47	0.32	0.07
Q-6	−1.16	−2.53	0.27	0.17
Q-7	−0.84	1.31	0.21	0.15
Q-8	0.52	1.14	0.25	0.19
ref 27	0.42		0.15	
ref 28	0.56		0.18	

[a]All values in mm/s.

The calculated Mössbauer parameters for models **Q-2**, **Q-3**, **Q-4**, and **Q-5** yield a multiline spectrum, due to the difference in the isomer shifts. This obviously differs from the experimental Mössbauer, which suggests two similar irons. Very good agreement with the experimental observation is found for models **Q-6**, **Q-7**, and **Q-8**. **Q-1** is the most reasonable of any of the closed-core models, however, the calculated isomer shift is too high and outside the typical error expected for such calculations (ca. 0.1 mm/s). Further, **Q-1** has already been eliminated based on the Fe−Fe distance being much too short. This leaves **Q-6**, **Q-7**, and **Q-8** as the most viable candidates for the structure of intermediate Q after the geometric and Mössbauer analysis.

3.2.4. XAS Pre-edge Spectra for MMOH$_Q$. Similar to the MMOH$_{ox}$ XAS spectra, the MMOH$_Q$ spectra are quite complex due to the ligand set and protein environment. However, in MMOH$_{ox}$, due to the two d^5 irons only excitations of β-electrons from the core to the valence shell are allowed. By contrast, the Fe(IV) d^4 configuration in MMO-Q features empty d-based molecular orbitals that can be reached by excitation from either a spin-up or a spin-down electron.

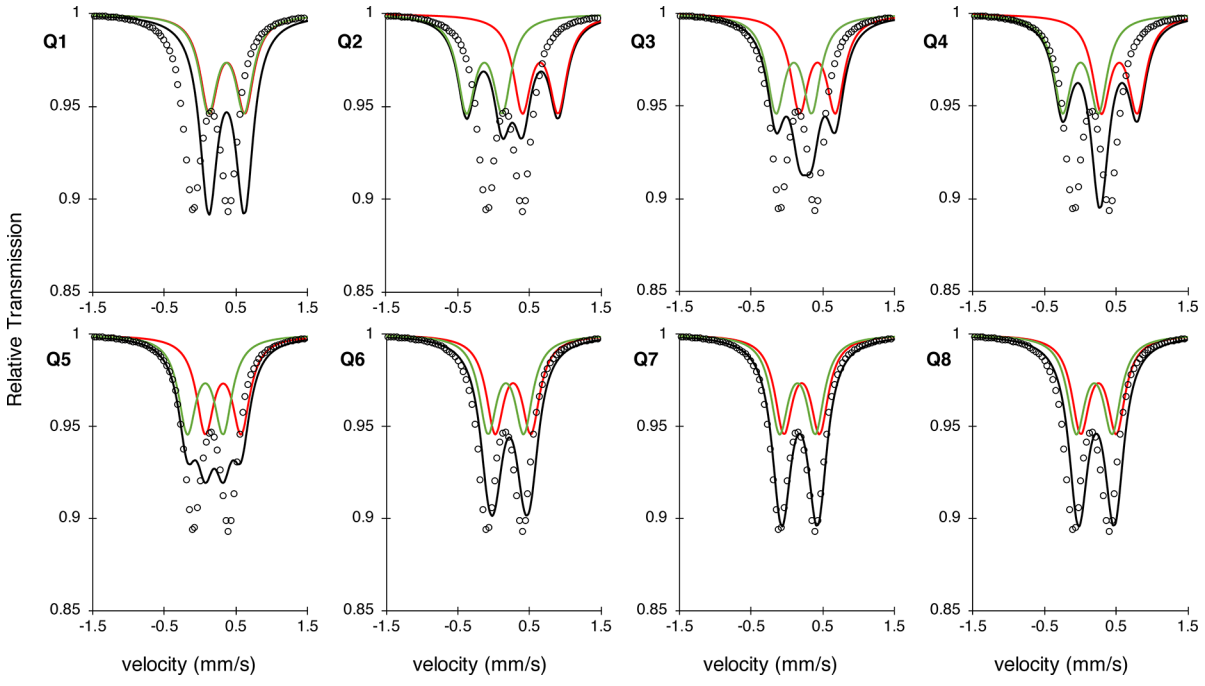

Figure 10. Simulated Mössbauer spectra of the two calculated isotope shifts (red, green) and their resulting spectrum (black), using the average of the experimental quadrupole splitting (0.5). The simulated spectrum using the experimental MMOH$_Q$ values (dots) is added to provide a visual comparison that allows judgment of which model represents the experiment most accurately.

https://doi.org/10.1021/jacs.1c01180
J. Am. Chem. Soc. 2021, 143, 6560−6577

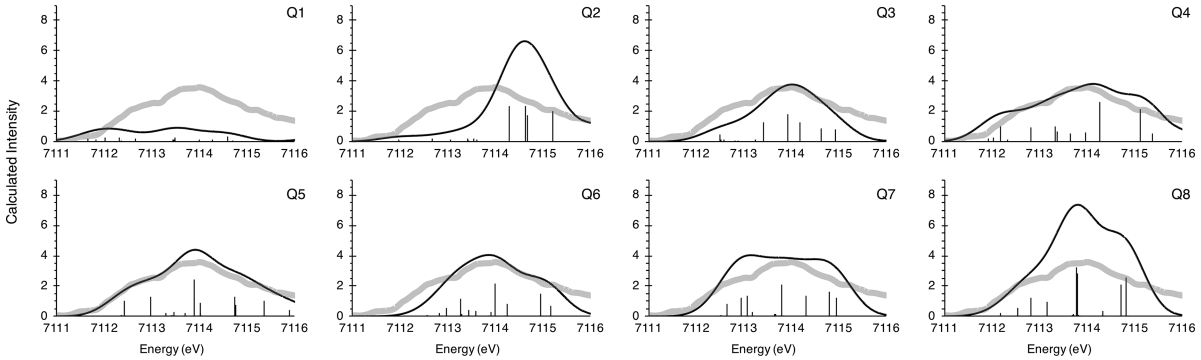

Figure 11. Calculated XAS pre-edge spectra for the $MMOH_Q$ models (black) on top of the experimental spectrum (gray).[27]

Table 6. Difference between Calculated and Experimental XAS Pre-edge Areas and IWAE of the $MMOH_Q$ Models

model	Q-1	Q-2	Q-3	Q-4	Q-5	Q-6	Q-7	Q-8	Exp[27]
IWAE (eV)	7112.8	7114.5	7113.9	7113.9	7113.7	7114.0	7113.8	7113.9	7114
Area	15.32	61.29	41.47	66.28	61.16	46.17	62.57	86.17	42.10

Consequently, in $MMOH_Q$ for the high spin S = 1 Fe(IV) configuration, significant spin polarization is expected to split the pre-edge into α/β d_{z^2} components.[96,107] As discussed elsewhere, this is a crude approximation to the true multiplet splittings that occur by exciting core electrons into empty orbitals in an open-shell system.[107] The treatment of spin-polarization in TDDFT is considered a "poor man's approximation" to the multiplet splitting,[96,107] as discussed multiple times.[27,108] A splitting is also observed for Fe(IV) S = 1 molecular model complexes (~0.6 eV).[27] Here caution has to be applied due to the differences in the local spin at the iron. Hence, first these model complex studies[27] are recalled in detail. It was found that pre-edge shapes and intensities directly reflect the similarity of the local electronic structure of the two metal sites. In closed-core models, the local geometries of the ions are very similar. Consequently, the transitions into the respective d orbitals of either iron site are very similar in energy, leading to six different energy transitions. If the two irons show differences in their local symmetry, the inequivalence of the metals lead to 12 different energy transitions. This is the case for the open-core model complexes, as well the protein models. Additionally, it was established in the model complexes that a lower local symmetry in the iron coordination geometry leads to an increase in the pre-edge intensity, as the p−d mixing allows for larger dipole contribution in the pre-edge, which is otherwise dominated by quadrupole contributions for more symmetric complexes.

The experimental XAS pre-edge shows an ~4 eV wide signal of high intensity, which consists of two grouped transitions, consistent with a distorted local octahedral O_h geometry at each iron. Several models show a similar shape (see Figure 11); however, clearly models **Q-5** and **Q-6** have the best visual agreement, in terms of both the energy and intensity distribution. To assess this more quantitatively, the calculated area, as well as the IWAE, is compared to the experiment in Table 6.

Looking at the calculated IWAEs, most models agree very well with experiment. For the areas, as discussed before, an error of at least 10% is expected. The best agreement is observed for model **Q-3**; however, the IWAE is far too low. **Q-6** is only marginally above the experimental intensity and, importantly, also in good agreement with the IWAE.

The comparison between similar models leads to the unexpected finding of a high intensity pre-edge for the closed-core model **Q-2**. As shown in Table 6, the pre-edge of **Q-2** is as intense as the signal of **Q-5**, without any terminal oxo ligands. The reason for the gain in intensity from model **Q-1** to model **Q-2** is the greater geometric distortion around the irons, and in particular the short Fe−O bonds at the Fe1 site, which provide a mechanism for enhanced p−d mixing via metal−ligand covalency.[109] A direct comparison is shown in Figure S14. The bond arrangement around the Fe1 of **Q-2** features much shorter ligand bonds, than in the Fe1 of **Q-1**. In summary, the best agreement with the XAS pre-edge experiment is observed for model **Q-6**, in terms of IWAE and pre-edge area. This ties well with the Mössbauer spectroscopy and the geometry analysis presented above.

In the following, the underlying nature of the XAS pre-edge transitions will be analyzed. Note that for the high spin Fe^{IV}, with a d^4 configuration and local spin state of 2, a total of six transitions per iron are expected, one α and five β transitions. Due to the increased asymmetry in the protein compared to the model complexes, for both diamond and closed cores, the two irons are sufficiently inequivalent such that all 12 transitions are found at different energies in the calculated pre-edge spectrum. An assignment for closed-core model **Q-1** and open-core model **Q-6** is presented in Figure S15. The transitions and the resulting orbital picture for the closed-core model **Q-1** and the open-core model **Q-6** are shown in Figure S15 (right panel).

At the lower energy side of the pre-edge of **Q-1**, transitions into the t_{2g} set are found. The signals from the two irons are overlapping and separated from the transitions into the e_g set. Next, in increasing energy, are the transitions into the d_{z^2} orbitals of each iron, with the transition into the Fe1 d_{z^2} orbital at lower energy. The transitions at the highest energy in the pre-edge region are excitations into the unoccupied $d_{x^2-y^2}$ orbitals of the respective iron. The α and β transitions to the $d_{x^2-y^2}$ are significantly split, which is attributed to spin polarization.[96,107] In **Q-6**, the same order of orbitals but more overlap of the signals is found. The transitions into the t_{2g} set are again found at lowest energy, followed by the transition

https://doi.org/10.1021/jacs.1c01180
J. Am. Chem. Soc. 2021, 143, 6560−6577

into the Fe2 d_{z^2} orbital. But here, the transitions into the Fe1 d_{z^2} orbital is found between the α and β transition to the $d_{x^2-y^2}$ orbitals. Using the assignment given by the XAS spectra, open- and closed-core model complexes can be compared. In the both models, the excitations with the highest energy are excitations into the unoccupied $d_{x^2-y^2}$ orbitals of the α and β subset. The d_{z^2} orbitals come at lower energy, and the t_{2g} orbitals, at the lowest. This has not been observed in open-core model complexes,[27] although the difference could arise from the difference in spin state. Yet, the spectroscopic trends between model complexes and protein models are very similar, both computationally and in experiment.

3.2.5. Raman Modes of MMOH$_Q$. One argument for the proposal of a closed core in MMOH$_Q$ has been derived from the experimental resonance Raman spectrum with labeled molecular oxygen.[17] In the experimental resonance Raman $^{16}O-^{18}O$ difference spectra, two signals are observed, one at 690/654 cm^{-1} and the other one at 556/533 cm^{-1}. While the latter was attributed to MMOH$_T$, which is formed after the reaction of MMOH$_Q$ with methane, it should be noted that the 556/533 cm^{-1} signal is also observed, when methane is not present, and the authors suggest these signals may also arrive from the spontaneous decay of Q in the absence of substrate.[17] We also note that, due the high noise level on the high energy side of the Raman spectrum, additional signals above 800 cm^{-1} may not have been captured. Hence, for the present analysis, we focus on the 690/654 cm^{-1} feature, acknowledging that additional experiments may be needed to positively assess the presence or absence of resonantly enhanced Raman features above 800 cm^{-1}.

Further, we acknowledge that the accurate calculation of the resonance Raman spectra of antiferromagnetically coupled transition metal dimers is a challenging undertaking. Given that most of the relevant information is contained in the shifts of the vibrational modes of the chromophore in the core, we have decided to study the nonresonant Raman spectra first in order to identify isotope sensitive vibrations in the various models and their relationship to the features observed in the resonance Raman experiment. As a consequence of this choice, the calculated intensities are of secondary importance for the comparison to experiment. One assumption taken here is that both oxygens from molecular O_2 are incorporated into the diiron core of MMOH$_Q$,[22] although not necessarily in the μ-oxo bridges.

Based on this reasoning, Raman modes of the constructed models are calculated and their difference spectra after in silico isotope labeling are investigated. However, the frequency shift upon isotope labeling is the same in both the resonant and nonresonant spectra. The resulting spectra are shown in Figure S16. Due to mechanical coupling of the core vibrations with the ligand environment (primarily involving the glutamate carboxyl ligands), the calculated Raman spectra are fairly complex. To partially resolve this issue, partial Hessians involving only the Fe_2O_2 core were calculated. There, the "pure" core modes are observed, as shown in Figure S17 which can be identified and then transferred to the full Hessian spectrum. A tabular summary is given in Table S7. The problem of overlapping modes when comparing the $^{16}O-^{18}O$ differences has been overcome by using mode tracking analysis. A summary of this analysis is given in Figure 12. Note that an additional layer of complexity in this analysis is that for open-core models of type **Q-6**, several possibilities for the insertion and cleavage of the labeled oxygen exist. Therefore, the three

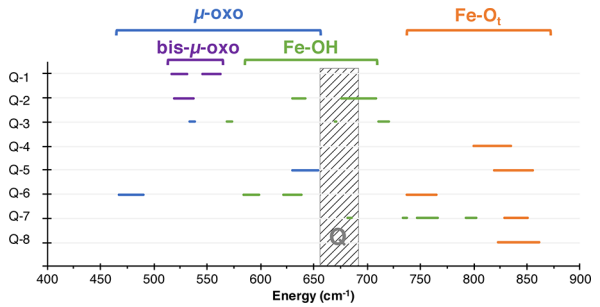

Figure 12. Overview on the calculated Raman frequencies (in cm^{-1}). Shifts are indicated as bars to lower frequencies. Modes that are predominantly along the Fe−O$_t$ are labeled in orange, modes following Fe−OH are shown in green, Fe−μO−Fe modes are in blue, and Fe−bis-μ-O−Fe modes are in purple. The experimental modes, assigned to MMOH$_Q$, are shown as a gray bar.

permutations of each of these modes have to be included in the analysis (see Figure S18).

In the following, each class of vibration is analyzed in terms of energy and isotope shifts, summarized in Table 7. Pure Fe−

Table 7. Characteristic Modes in the Non-Resonant Raman $^{16-18}O$ Difference Spectra and Their Respective Shifts, Sorted by the Motif[a]

	^{16}O min (cm^{-1})	^{16}O max (cm^{-1})
Fe−μO−Fe	490	654
Fe−bis-μ-O−Fe	532	563
Fe−OH	599	802
Fe−O$_t$	765	874

[a]Note that for model **Q-6**, where different labeling patterns were probed, multiple entries to the same mode with different shifts are obtained.

O$_t$ stretches are observed around 850 cm^{-1} (model **Q-4**, model **Q-8**), but can be shifted down to 765 cm^{-1} by hydrogen bonding (model **Q-6**, shown in orange in Figure 12). While in model **Q-8** the isotope shift is −39 cm^{-1}, in model **Q-7** a shift of −20 cm^{-1} is found. Depending on the combination of labeled oxygen, the isotope shift in model **Q-6** is −4 cm^{-1} or −27 cm^{-1}.

Pure Fe−OH stretches are uncommon, because of the amount of hydrogen bond acceptors around the Fe_2O_2 site. The least hydrogen bound example can be found in model **Q-2** at around 700 cm^{-1}. This transition has an isotope shift of −33 cm^{-1}. Hydrogen bound Fe−OH stretches are observed in model **Q-3** at 720 cm^{-1}, with an isotope shift of −10 cm^{-1}. Fe−μO−Fe shifts are observed below 500 cm^{-1} (model **Q-6**), but can be found at higher frequencies depending on the involved ligand. Combinations of Fe−OH and Fe−μO−Fe stretches can be found at 654 cm^{-1} in model **Q-6**, with an isotope shift of −24 cm^{-1}. This depends on the actual positions of the labels as shown in Figure S18.

Modes involving Fe−μO_2−Fe are predominantly observed in model **Q-1**, in an energy range between 532 and 562 cm^{-1}. These modes can be described as symmetric and asymmetric "breathing" modes. They combine with the glutamate ligand vibrations and hence are quite a bit lower than analogous model complexes. These vibration modes have calculated isotope shifts of −14 and −17 cm^{-1}, respectively.

In the range of the experimentally observed MMOH$_Q$ signals, between 650 and 700 cm^{-1} two types of signals can

https://doi.org/10.1021/jacs.1c01180
J. Am. Chem. Soc. 2021, 143, 6560−6577

Table 8. Summary of the Experimental Criteria for the Evaluation of the $MMOH_Q$ Models[a]

	Geometry	Mössbauer	XAS pre-edge		Raman	
model	Δd(Fe−Fe) (Å)	$\Delta\delta$ (mm/s)	ΔIWAE (eV)	Area Ratio	$\Delta\nu$ (cm^{-1})	$\Delta\delta$ (cm^{-1})
Q-1	−0.60	**0.01**	−0.87	0.36	−127.27	−19.26
Q-2	−0.56	0.79	0.57	1.46	18.25	**-3.17**
Q-3	−0.42	0.33	−0.10	**0.99**	30.65	−25.63
Q-4	−0.37	0.54	**−0.04**	1.57	144.72	**-1.28**
Q-5	**-0.20**	0.26	**-0.01**	1.45	−35.74	−11.21
Q-6	**-0.19**	**0.10**	−0.79	**1.10**	−51.05	−18.19
Q-7	0.45	**0.07**	−0.16	1.49	**−4.16**	−32.41
Q-8	0.28	**0.05**	**−0.08**	2.05	171.85	**2.78**

[a]Values in bold indicate agreement with experiment within the target accuracy as established before.

be found. These include mostly combination bands between the Fe−μO−Fe stretches (model **Q-5**) and Fe−OH stretches (model **Q-2**). These modes have an isotope shift of −25 and −32 cm^{-1}, respectively (see Figure S19 for depiction of these modes). Larger isotope shifts, like the 36 cm^{-1} observed in the experimental $MMOH_Q$ signal from 690 to 654 cm^{-1}, are only observed for Fe−O_t stretches between 650 and 700 cm^{-1}, for example for model **Q-5**, model **Q-6**, and model **Q-8**. For the Fe−μO−Fe and Fe−OH combination bands that lie in the experimental $MMOH_Q$ range, maximum shifts of −18 to −25 cm^{-1} are observed.

In conclusion, hydrogen bonding and its modulation of the Raman modes are an essential aspect of the $MMOH_Q$ Raman spectra. In the presented models, no perfect agreement with the experimental energy range and isotope shift was found. It seems plausible that the experimentally observed features can be attributed to a combination of an Fe−OH and Fe−μO−Fe mode.

3.2.6. Combining Evidence on $MMOH_Q$. A summary of all previously discussed criteria for the $MMOH_Q$ models is given in Table 8. From the geometry analysis it was shown that only open core models agree with the revisited EXAFS distance,[28] albeit the μ-oxo bridged models are 0.2 Å too short. Among the open models, models **Q-6** and **Q-8** showed the best agreement in the Mössbauer simulations. In the analysis of XAS pre-edges, it was shown that only models with terminal oxo groups reproduce the intense pre-edge features. Hydrogen bonding modulates the intensity and position of the pre-edge, which suggests that there are many more options than the selection presented here. The best agreement for IWAE, area, and pre-edge shape is observed for models **Q-5** and **Q-6**. In the Raman experiment, the best agreement for isotope shifts is observed for terminal oxo stretches, while signals in the experimental range originate from terminal hydroxo stretches in **Q-2** or μ-oxo stretches in **Q-5**. It was shown that hydrogen bonding allows for the modes spanning the whole diiron core, which improves agreement with experiment in terms of energy and isotope sensitivity. Combining the results from Mössbauer, XAS, and Raman calculations with the analysis of the geometry indicates that model **Q-6** is the structure that is most consistent with the experimental data for $MMOH_Q$.

3.3. Discussion. In the following we discuss the extent to which the $MMOH_Q$ models developed in this work can be compared with synthetic high valent model complexes,[27,34,105] and we explore the possible implications of the present results for the reaction mechanism of sMMO.

3.3.1. Comparison to Model Complexes. Biomimetic model complexes can be used as structural models, to explore the electronic structure of the diiron core, or as functional models, stabilizing relevant Fe(IV) oxo motifs to investigate the reactivity and plausible mechanisms. Structural models[105] (Figure S1) have been discussed extensively in connection with the XAS pre-edge analysis.[27] It should be recalled however that the spin states of the irons in these model complexes do not necessarily reflect the electronic structure of the protein, as they are all $S = 1$. Hence, only some of the findings in the synthetic complexes are transferable to our comparisons between closed- and open-conformations of the QM/MM models. One common feature is the orientation of the d_{z^2} orbital in the closed-core QM/MM models (**Q-1**) and closed-core model complexes (complex 3 in ref 27). Resulting from this agreement in the electronic structure, also a reasonable agreement in the spectroscopic properties is observed:[27] both **Q-1** and the closed-core model complex feature a low intensity pre-edge, with comparable IWAE. The Mössbauer results indicate two similar irons in both cases.

In the case of the open-core QM/MM models and the open-core model complex (Figure S1, model 4),[27] a direct comparison is more complicated. One similarity is the behavior of the d_{z^2} orbitals of the two irons in QM/MM models and model complexes. In both cases the d_{z^2} orbital of the individual irons are orthogonal to each other. However, since the terminal oxo ligand in **Q-5** is oriented in the same way as the terminal water ligand in **Q-1**, no changes in the orientation of the d_{z^2} orbital were found here. Instead, the d_{z^2} orbital of the other iron, Fe2, is oriented along the Fe-μ-oxo/Fe-OGlu209 bond. As discussed for the model complexes, this orthogonality behavior is controlled by the strongest σ type metal−ligand interaction. In the model complexes, this is unambiguously the Fe=O σ interaction. However, in the protein the glutamate oxygens compete with the μ-oxo and terminal oxo ligands. Hence, this reordering is not observed for all open QM/MM models. Another difference to the synthetic diiron Fe(IV) complexes is the d orbital order for the iron sites. In the synthetic model the identity of the LUMO differs for the two irons, whereas in the QM/MM open-core models both sites share the same identity of the LUMO. One possible explanation could be the similarity of the two iron sites in the synthetic models, as reflected by Mössbauer spectroscopy: here the open-core model complex shows two very different irons, while the QM/MM models of the enzymatic active site (**Q-5** and **Q-6**) show very similar irons. In conclusion, the open-core QM/MM models of $MMOH_Q$ and the available synthetic open-core analogues are less comparable than the closed-core versions and hence the transferability of observations based on synthetic open-core complexes to the actual enzyme should be considered with caution.

https://doi.org/10.1021/jacs.1c01180
J. Am. Chem. Soc. 2021, 143, 6560−6577

Scheme 1. Possible $MMOH_{red}$ to $MMOH_{ox}$ Transitions for Open Cores of $MMOH_Q$[a]

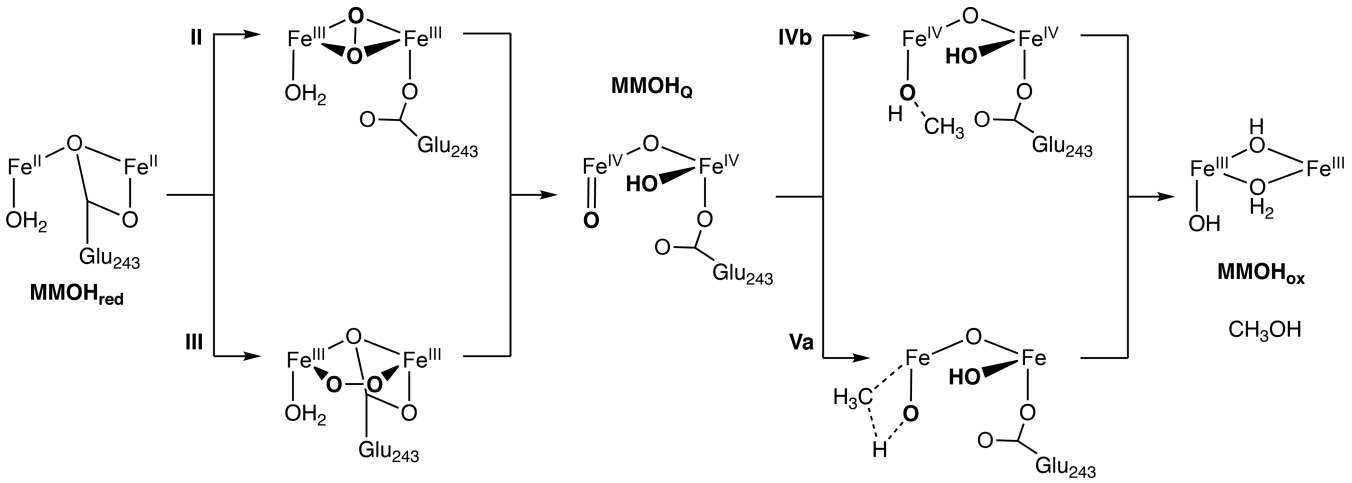

[a]Note that for transition states explicit steps are omitted for clarity.

Aside from these structural models, the reactivity of high valent iron complexes has been studied in great detail on mononuclear iron(IV) complexes. Of course, with two irons, MMOH differs from the models discussed in these studies. However, for the open-core models of $MMOH_Q$ the d_{z^2} orbital is oriented along the Fe−O moiety, making it comparable to the mononuclear iron complexes. Yet the fact that the d_{z^2} is orthogonal to the other moiety may have implications in the reactivity or selectivity. The CH reactivity was probed using model complexes featuring different iron oxo units. A steep increase in reactivity for the models with an Fe(IV)═O moiety was observed.[34] While Fe(IV) diiron complexes are rare,[34,110] mononuclear Fe(IV) intermediates are studied extensively,[111] especially concerning the influence of the iron spin states on the reactivity.[112,113] One central question is the influence of the electronic structure at the Fe−O moiety on the reactivity and mechanism of the C−H abstraction. For one, depending on the local spin state of the iron, the substrate interacts with either a triplet or quintet ground state. On the other hand, the local geometry of the electron accepting orbitals at the iron leads to different possibilities as to how the reaction can be rationalized.[114] Depending on whether these are of σ- or π-type, these are referred to as σ- or π-channels.[115] If the electron is transferred into the iron d_{z^2}, which can be understood as σ-antibonding in the Fe−O bond, this is referred to as the σ-channel. In the quintet state, the d_{z^2} orbital is the HOMO; hence it is energetically favorable to transfer the electron here. If on the other hand, the electron is inserted into the iron d_{xz} or d_{yz} orbitals, this is referred to as the π-channel. These are the SOMOs in the triplet state and, hence, preferred targets here. Both channels lead to different transition state geometries, i.e. a linear or bent Fe−O-substrate coordinate. Such detailed studies are beyond the scope of the present study. However, the established concepts can be placed in the context of our present study and combined with existing discussion on the MMOH mechanism.

3.3.2. Implications for Reaction Mechanisms Involving $MMOH_Q$. In the following, the mechanism of the MMOH active site is discussed, as far as $MMOH_Q$ is involved. A detailed computational investigation of possible mechanisms is outside the scope of the present work and will be reported in future studies. While the results presented above are in favor of an open-core assignment for $MMOH_Q$, the majority of mechanistic ideas and computational mechanistic studies in the literature have been discussed on the basis of a closed-core configuration for $MMOH_Q$. Hence, these are reviewed before we discuss the implications of an open core for $MMOH_Q$.

The structure of the $MMOH_Q$ has immediate implications for the catalytic steps leading to the formation of $MMOH_Q$ and for methane activation. $MMOH_Q$ is formed by decay of the $MMOH_P$, the exact structure of which remains a subject of controversy. $MMOH_P$ is formed by O_2 insertion of $MMOH_{red}$. There are several plausible motifs for $MMOH_P$,[8] as shown in Scheme S1. Similar to the structure, the mechanism of $MMOH_P$ to $MMOH_Q$ conversion is under debate.[8,24] Yet, based on the information gained on $MMOH_Q$, specific possibilities have been formulated on how the transition from $MMOH_P$ to $MMOH_Q$ might occur (Scheme S1). Based on analogy to the cytochrome P450 monooxygenase,[116] a similar mechanism (**I**) was proposed for MMOH.[117] However, this is in conflict with the resonance Raman experiment[22] showing that both oxygens from molecular oxygen are incorporated into the diiron core of $MMOH_Q$. Yet, it was found that the proton transfer was not part of the rate-determining step,[118] which led to the proposal of a proton independent mechanism (**II**). Upon reexamining the role of protons in the $MMOH_P$ to $MMOH_Q$ transition, it was found that proton transfer promotes O−O bond cleavage,[119] upon which a matching mechanism was proposed (**III**). These have been modeled computationally.[52,68] Comparisons to other nonheme iron enzymes were made.[39]

All of these considerations assume a bis-μ-oxo core for $MMOH_Q$. However, it is plausible that these mechanisms could result in an open-core geometry, depending on how the O−O bond is broken and how the oxygens reassemble. Homolytic cleavage of the oxygen bond in a trans bound O_2 leads to a bis-μ-oxo core, while heterolytic cleavage of the O−O bond might result in a terminal-oxo/μ-oxo core.

Similar considerations can be made for the methane activation step or $MMOH_Q$ decay. It is established by kinetic studies that other steps than the C−H cleavage are rate limiting in the enzymatic reaction.[22] The large kinetic isotope effect observed for the methane activation step was interpreted as tunneling of the hydrogen atom during the abstraction

https://doi.org/10.1021/jacs.1c01180
J. Am. Chem. Soc. 2021, 143, 6560−6577

process.[120,121] So far there is evidence for two types of mechanisms: radical mechanisms[50,122−128] or concerted mechanisms.[129−131] These were further analyzed using computational studies. The results can be summarized into iron-centered and oxygen-centered mechanisms (Scheme S2). Mechanism **IVa** is characterized by rearrangement of the bis-μ-oxo core into an Fe(IV) oxo radical, which then abstracts a proton from the substrate. The remaining CH_3 radical is then coordinated to the iron, and eventually recombined to methanol. This mechanism was suggested by Siegbahn and co-workers.[35,36,38] One could also imagine an oxygen centered variance of this mechanism, then termed the radical rebound mechanism: **IVb**.[36,38,51] Here, a CH bond of the substrate is broken by a μ-oxo, leading to a CH_3 radical that rebounds with the same oxygen. Mechanism **Va**, advocated by the Yoshizawa group,[42−49,69] is best described as a concerted nonradical mechanism, initiated by a proton transfer to a μ-oxo while stabilizing the CH_3 group at the iron, before recombination to methanol. A variant of that mechanism was termed the nonsynchronous concerted pathway (**Vb**), explored by Friesner and Lippard.[61,64,65,131] Here, the CH_3 group is stabilized by the protein environment, not the iron. Hence this mechanism can be viewed as oxygen-centered.

For the open-core models in this study, several of these mechanisms are plausible. The spontaneous opening of the μ-oxo bond is less likely for models with only one μ-oxo bond, especially for the glutamate bridging ligands. The other μ-oxo centered mechanisms could be transferred to the mono-μ-oxo ligands as well. However, as the open models feature terminal oxo ligands, it is highly likely that the terminal oxo is a central aspect of the mechanism, as it is in model complexes.

For the presented case of an open model, possible mechanisms are collected in Scheme 1. Upon heterolytic cleavage of the dioxygen bond, the terminal oxo ligand is formed. The bridge could be protonated either during the cleavage or subsequently. Similar to model complexes the terminal oxo is expected to be the reactive group in the methane activation step, following a similar reactivity as for the mononuclear iron complexes. Both a radical mechanism, based on the oxyl character of the Fe═O group, or a concerted mechanism seem plausible for the open models. In computational studies of model complexes, it was found that the reactivity of the Fe(IV)═O unit is modulated by the ligand to the second iron,[132] similar to what has been discussed for the Raman calculations before. Further examination of these distinct possibilities will be pursued in the future using the here developed QM/MM setup.

4. CONCLUSIONS

This study presented a wide range of possible models for the $MMOH_{ox}$ and $MMOH_Q$ intermediates of soluble methane monooxygenase, focusing on elucidating in great detail the possible connections between structural features and spectroscopic properties. The approach followed in this work emphasizes the construction of high-level QM/MM models that explicitly take into account the protein environment, combined with high-level quantum chemical calculations of spectroscopic parameters that enable reliable evaluation of the computational models against experimental information on the distinct catalytic intermediates. We have evaluated models for both intermediates on the basis of experimental geometric constraints, Mössbauer spectroscopy, and X-ray absorption spectroscopy. Specifically for $MMOH_Q$ we have also studied in detail the vibrational properties of the different computational models in connection to resonance Raman data.

A central question concerning the nature of $MMOH_Q$ is the structural type of the diiron core, i.e. whether it is a closed core, with at least two bridging oxo groups leading to an Fe_2O_2 "diamond" topology, or whether it adopts a more open-core configuration, which has been associated in synthetic model chemistry with higher reactivity. A major experimental constraint is the Fe−Fe distance of $MMOH_Q$ as deduced by recent EXAFS measurements, which revised the incorrect short distance assumed in prior studies. We demonstrate that the EXAFS distance agrees only with open-core QM/MM models of $MMOH_Q$. The simulation of the Mössbauer parameters shows agreement for several open-core models. Here, the local geometry of the iron and the hydrogen bonding between the bridges and surrounding amino acids are shown to have a great effect. Analysis of XAS pre-edge data confirms that a closed core without terminal oxo ligands does not lead to the observed pre-edge intensity. With terminal oxo ligands, the necessary intensity is achieved. Here again, the protonation state is of great importance to the shape and intensity of the pre-edge. Importantly, we show that the previous analysis of the resonance Raman experiment was limited in its initial assumptions,[22] and that the data can be fully consistent with an open-core formulation of $MMOH_Q$ if hydrogen bonding between the terminal Fe ligands is considered.

Overall, the present analysis points squarely toward an open-core topology for the $MMOH_Q$ intermediate. It offers concrete reinterpretations of experimental data, reconciling suggestions that until now seemed to be in conflict. Moreover, the spectroscopically consistent open-core structure of $MMOH_Q$ is finally brought in line with the enhanced reactivity of this type of core, as observed in synthetic analogues. The present conclusions and computational models will form the basis for more reliable investigations of the catalytic mechanism of the enzyme in the future.

■ ASSOCIATED CONTENT

Supporting Information

The Supporting Information is available free of charge at https://pubs.acs.org/doi/10.1021/jacs.1c01180.

Figures S1−S19, Tables S1−S7, Schemes S1 and S2 (PDF)

■ AUTHOR INFORMATION

Corresponding Authors

Serena DeBeer − *Max Planck Institute for Chemical Energy Conversion, 45470 Mülheim an der Ruhr, Germany;* orcid.org/0000-0002-5196-3400; Email: serena.debeer@cec.mpg.de

Frank Neese − *Max-Planck-Institut für Kohlenforschung, 45470 Mülheim an der Ruhr, Germany;* orcid.org/0000-0003-4691-0547; Email: frank.neese@kofo.mpg.de

Authors

Christine E. Schulz − *Max-Planck-Institut für Kohlenforschung, 45470 Mülheim an der Ruhr, Germany;* orcid.org/0000-0002-0340-6212

Rebeca G. Castillo − *Max Planck Institute for Chemical Energy Conversion, 45470 Mülheim an der Ruhr, Germany*

Dimitrios A. Pantazis − *Max-Planck-Institut für Kohlenforschung, 45470 Mülheim an der Ruhr, Germany;* orcid.org/0000-0002-2146-9065

Complete contact information is available at: https://pubs.acs.org/10.1021/jacs.1c01180

Notes

The authors declare no competing financial interest.

■ ACKNOWLEDGMENTS

The Max Planck Society is gratefully acknowledged for funding. We thank Drs. E. Bill, G. E. Cutsail III, and R. Bjornsson for helpful discussions. C.E.S. and R.G.C. acknowledge the IMPRS-RECHARGE for funding.

■ REFERENCES

(1) Hanson, R. S.; Hanson, T. E. Methanotrophic bacteria. *Microbiol. Rev.* **1996**, *60*, 439−471.
(2) Ross, M. O.; Rosenzweig, A. C. A tale of two methane monooxygenases. *JBIC, J. Biol. Inorg. Chem.* **2017**, *22*, 307−319.
(3) Banerjee, R.; Jones, J. C.; Lipscomb, J. D. Soluble methane monooxygenase. *Annu. Rev. Biochem.* **2019**, *88*, 409−431.
(4) Colby, J.; Stirling, D. I.; Dalton, H. The soluble methane mono-oxygenase of Methylococcus capsulatus (Bath). Its ability to oxygenate n-alkanes, n-alkenes, ethers, and alicyclic, aromatic and heterocyclic compounds. *Biochem. J.* **1977**, *165*, 395−402.
(5) Wallar, B. J.; Lipscomb, J. D. Dioxygen activation by enzymes containing binuclear non-heme iron clusters. *Chem. Rev.* **1996**, *96*, 2625−2658.
(6) Stanley, S.; Prior, S.; Leak, D.; Dalton, H. Copper stress underlies the fundamental change in intracellular location of methane mono-oxygenase in methane-oxidizing organisms: studies in batch and continuous cultures. *Biotechnol. Lett.* **1983**, *5*, 487−492.
(7) Semrau, J. D.; DiSpirito, A. A.; Yoon, S. Methanotrophs and copper. *FEMS Microbiol. Rev.* **2010**, *34*, 496−531.
(8) Tinberg, C. E.; Lippard, S. J. Dioxygen Activation in Soluble Methane Monooxygenase. *Acc. Chem. Res.* **2011**, *44*, 280−288.
(9) Sirajuddin, S.; Rosenzweig, A. C. Enzymatic oxidation of methane. *Biochemistry* **2015**, *54*, 2283−2294.
(10) Merkx, M.; Kopp, D. A.; Sazinsky, M. H.; Blazyk, J. L.; Müller, J.; Lippard, S. J. Dioxygen Activation and Methane Hydroxylation by Soluble Methane Monooxygenase: A Tale of Two Irons and Three Proteins. *Angew. Chem., Int. Ed.* **2001**, *40*, 2782−2807.
(11) Kim, H.; An, S.; Park, Y. R.; Jang, H.; Yoo, H.; Park, S. H.; Lee, S. J.; Cho, U.-S. MMOD-induced structural changes of hydroxylase in soluble methane monooxygenase. *Science advances* **2019**, *5*, No. eaax0059.
(12) Lee, S. J.; McCormick, M. S.; Lippard, S. J.; Cho, U.-S. Control of substrate access to the active site in methane monooxygenase. *Nature* **2013**, *494*, 380−384.
(13) Jones, J. C.; Banerjee, R.; Shi, K.; Aihara, H.; Lipscomb, J. D. Structural Studies of the Methylosinus trichosporium OB3b Soluble Methane Monooxygenase Hydroxylase and Regulatory Component Complex Reveal a Transient Substrate Tunnel. *Biochemistry* **2020**, *59*, 2946−2961.
(14) Rosenzweig, A. C.; Frederick, C. A.; Lippard, S. J.; Nordlund, P. Crystal-structure of a bacterial nonheme iron hydroxylase that catalyzes the biological oxidation of methane. *Nature* **1993**, *366*, 537−543.
(15) Fox, B.; Surerus, K.; Münck, E.; Lipscomb, J. D. Evidence for a mu-oxo-bridged binuclear iron cluster in the hydroxylase component of methane monooxygenase. Mössbauer and EPR studies. *J. Biol. Chem.* **1988**, *263*, 10553−10556.
(16) Kovaleva, E.; Neibergall, M.; Chakrabarty, S.; Lipscomb, J. D. Finding intermediates in the O2 activation pathways of non-heme iron oxygenases. *Acc. Chem. Res.* **2007**, *40*, 475−483.
(17) Banerjee, R.; Proshlyakov, Y.; Lipscomb, J. D.; Proshlyakov, D. A. Structure of the key species in the enzymatic oxidation of methane to methanol. *Nature* **2015**, *518*, 431−434.
(18) Elango, N.; Radhakrishnan, R.; Froland, W. A.; Wallar, B. J.; Earhart, C. A.; Lipscomb, J. D.; Ohlendorf, D. H. Crystal structure of the hydroxylase component of methane monooxygenase from Methylosinus trichosporium OB3b. *Protein Sci.* **1997**, *6*, 556−568.
(19) Han, W.-G.; Noodleman, L. Structural model studies for the high-valent intermediate Q of methane monooxygenase from broken-symmetry density functional calculations. *Inorg. Chim. Acta* **2008**, *361*, 973−986.
(20) Que, L.; Tolman, W. B. Biologically inspired oxidation catalysis. *Nature* **2008**, *455*, 333−340.
(21) Rinaldo, D.; Philipp, D. M.; Lippard, S. J.; Friesner, R. A. Intermediates in dioxygen activation by methane monooxygenase: A QM/MM study. *J. Am. Chem. Soc.* **2007**, *129*, 3135−3147.
(22) Shu, L.; Nesheim, J. C.; Kauffmann, K.; Münck, E.; Lipscomb, J. D.; Que, L. An Fe2(IV)(O)2 Diamond Core Structure for the Key Intermediate Q of Methane Monooxygenase. *Science* **1997**, *275*, 515−518.
(23) Siegbahn, P. E. M.; Crabtree, R. H.; Nordlund, P. Mechanism of methane monooxygenase - a structural and quantum chemical perspective. *JBIC, J. Biol. Inorg. Chem.* **1998**, *3*, 314−317.
(24) Wallar, B. J.; Lipscomb, J. D. Dioxygen activation by enzymes containing binuclear non-heme iron clusters. *Chem. Rev.* **1996**, *96*, 2625−2657.
(25) Lee, S.-K.; Nesheim, J. C.; Lipscomb, J. D. Transient intermediates of the methane monooxygenase catalytic cycle. *J. Biol. Chem.* **1993**, *268*, 21569−21577.
(26) Lee, S. K.; Fox, B. G.; Froland, W. A.; Lipscomb, J. D.; Munck, E. A transient intermediate of the methane monooxygenase catalytic cycle containing an FeIVFeIV cluster. *J. Am. Chem. Soc.* **1993**, *115*, 6450−6451.
(27) Castillo, R. G.; Banerjee, R.; Allpress, C. J.; Rohde, G. T.; Bill, E.; Que, L., Jr.; Lipscomb, J. D.; DeBeer, S. High-Energy-Resolution Fluorescence-Detected X-ray Absorption of the Q Intermediate of Soluble Methane Monooxygenase. *J. Am. Chem. Soc.* **2017**, *139*, 18024−18033.
(28) Cutsail, G. E.; Banerjee, R.; Zhou, A.; Que, L.; Lipscomb, J. D.; DeBeer, S. High-Resolution Extended X-ray Absorption Fine Structure Analysis Provides Evidence for a Longer Fe···Fe Distance in the Q Intermediate of Methane Monooxygenase. *J. Am. Chem. Soc.* **2018**, *140*, 16807−16820.
(29) Friedle, S.; Reisner, E.; Lippard, S. J. Current challenges of modeling diiron enzyme active sites for dioxygen activation by biomimetic synthetic complexes. *Chem. Soc. Rev.* **2010**, *39*, 2768−2779.
(30) Tshuva, E. Y.; Lippard, S. J. Synthetic models for non-heme carboxylate-bridged diiron metalloproteins: strategies and tactics. *Chem. Rev.* **2004**, *104*, 987−1012.
(31) Xue, G.; Fiedler, A. T.; Martinho, M.; Münck, E.; Que, L. Insights into the P-to-Q conversion in the catalytic cycle of methane monooxygenase from a synthetic model system. *Proc. Natl. Acad. Sci. U. S. A.* **2008**, *105*, 20615−20620.
(32) Que, L., Jr.; Tolman, W. B. Bis (μ-oxo) dimetal "Diamond" Cores in Copper and Iron Complexes Relevant to Biocatalysis. *Angew. Chem., Int. Ed.* **2002**, *41*, 1114−1137.
(33) Jasniewski, A. J.; Que, L., Jr. Dioxygen activation by nonheme diiron enzymes: Diverse dioxygen adducts, high-valent intermediates, and related model complexes. *Chem. Rev.* **2018**, *118*, 2554−2592.
(34) Xue, G.; De Hont, R.; Münck, E.; Que, L. Million-fold activation of the [Fe2(μ-O)2] diamond core for C-H bond cleavage. *Nat. Chem.* **2010**, *2*, 400−405.
(35) Siegbahn, P. E. M.; Crabtree, R. H. Mechanism of C-H activation by diiron methane monooxygenases: Quantum chemical studies. *J. Am. Chem. Soc.* **1997**, *119*, 3103−3113.
(36) Siegbahn, P. E. M. Theoretical model studies of the iron dimer complex of MMO and RNR. *Inorg. Chem.* **1999**, *38*, 2880−2889.

(37) Siegbahn, P. E. M.; Blomberg, M. R. A. Transition-metal systems in biochemistry studied by high-accuracy quantum chemical methods. *Chem. Rev.* **2000**, *100*, 421−437.
(38) Siegbahn, P. E. M. O-O bond cleavage and alkane hydroxylation in methane monooxygenase. *JBIC, J. Biol. Inorg. Chem.* **2001**, *6*, 27−45.
(39) Siegbahn, P. E. M. A comparison of dioxygen bond-cleavage in ribonucleotide reductase (RNR) and methane monooxygenase (MMO). *Chem. Phys. Lett.* **2002**, *351*, 311−318.
(40) Lovell, T.; Li, J.; Noodleman, L. Density functional studies of oxidized and reduced methane monooxygenase. Optimized geometries and exchange coupling of active site clusters. *Inorg. Chem.* **2001**, *40*, 5251−5266.
(41) Lovell, T.; Han, W. G.; Liu, T. Q.; Noodleman, L. A structural model for the high-valent intermediate Q of methane monooxygenase from broken-symmetry density functional and electrostatics calculations. *J. Am. Chem. Soc.* **2002**, *124*, 5890−5894.
(42) Yoshizawa, K.; Hoffmann, R. Dioxygen binding to dinuclear iron centers on methane monooxygenase models. *Inorg. Chem.* **1996**, *35*, 2409−2410.
(43) Yoshizawa, K.; Ohta, T.; Yamabe, T.; Hoffmann, R. Dioxygen cleavage and methane activation on diiron enzyme models: A theoretical study. *J. Am. Chem. Soc.* **1997**, *119*, 12311−12321.
(44) Yoshizawa, K.; Yamabe, T.; Hoffmann, R. Possible intermediates for the conversion of methane to methanol on dinuclear iron centers of methane monooxygenase models. *New J. Chem.* **1997**, *21*, 151−161.
(45) Yoshizawa, K.; Yokomichi, Y.; Shiota, Y.; Ohta, T.; Yamabe, T. Density functional study on possible peroxo form of non-heme diiron enzyme model. *Chem. Lett.* **1997**, *26*, 587−588.
(46) Yoshizawa, K. Two-step concerted mechanism for alkane hydroxylation on the ferryl active site of methane monooxygenase. *JBIC, J. Biol. Inorg. Chem.* **1998**, *3*, 318−324.
(47) Yoshizawa, K.; Shiota, Y.; Yamabe, T. Methane-methanol conversion by MnO+, FeO+, and CoO+: A theoretical study of catalytic selectivity. *J. Am. Chem. Soc.* **1998**, *120*, 564−572.
(48) Yoshizawa, K.; Suzuki, A.; Shiota, Y.; Yamabe, T. Conversion of methane to methanol on diiron and dicopper enzyme models of methane monooxygenase: A theoretical study on a concerted reaction pathway. *Bull. Chem. Soc. Jpn.* **2000**, *73*, 815−827.
(49) Yoshizawa, K. Methane inversion on transition metal ions: a possible mechanism for stereochemical scrambling in metal-catalyzed alkane hydroxylations. *J. Organomet. Chem.* **2001**, *635*, 100−109.
(50) Huang, S. P.; Shiota, Y.; Yoshizawa, K. DFT study of the mechanism for methane hydroxylation by soluble methane monooxygenase (sMMO): effects of oxidation state, spin state, and coordination number. *Dalton Trans.* **2013**, *42*, 1011−1023.
(51) Basch, H.; Mogi, K.; Musaev, D. G.; Morokuma, K. Mechanism of the methane -> methanol conversion reaction catalyzed by methane monooxygenase: A density functional study. *J. Am. Chem. Soc.* **1999**, *121*, 7249−7256.
(52) Torrent, M.; Mogi, K.; Basch, H.; Musaev, D. G.; Morokuma, K. A density functional study of possible intermediates of the reaction of dioxygen molecule with non-heme iron complexes. 1. N-side versus O-side mechanism with water-free model. *J. Phys. Chem. B* **2001**, *105*, 8616−8628.
(53) Basch, H.; Musaev, D. G.; Morokuma, K. A density functional study of the completion of the methane monooxygenase catalytic cycle. Methanol complex to MMOH resting state. *J. Phys. Chem. B* **2001**, *105*, 8452−8460.
(54) Basch, H.; Musaev, D. G.; Mogi, K.; Morokuma, K. Theoretical studies on the mechanism of the methane -> methanol conversion reaction catalyzed by methane monooxygenase: O-side vs N-side mechanisms. *J. Phys. Chem. A* **2001**, *105*, 3615−3622.
(55) Torrent, M.; Musaev, D. G.; Morokuma, K. The flexibility of carboxylate ligands in methane monooxygenase and ribonucleotide reductase: A density functional study. *J. Phys. Chem. B* **2001**, *105*, 322−327.
(56) Musaev, D. G.; Basch, H.; Morokuma, K. Theoretical study of the mechanism of alkane hydroxylation and ethylene epoxidation reactions catalyzed by diiron bis-oxo complexes. The effect of substrate molecules. *J. Am. Chem. Soc.* **2002**, *124*, 4135−4148.
(57) Torrent, M.; Vreven, T.; Musaev, D. G.; Morokuma, K.; Farkas, O.; Schlegel, H. B. Effects of the protein environment on the structure and energetics of active sites of metalloenzymes. ONIOM study of methane monooxygenase and ribonucleotide reductase. *J. Am. Chem. Soc.* **2002**, *124*, 192−193.
(58) Torrent, M.; Musaev, D. G.; Basch, H.; Morokuma, K. Computational studies of reaction mechanisms of methane monooxygenase and ribonucleotide reductase. *J. Comput. Chem.* **2002**, *23*, 59−76.
(59) Dunietz, B. D.; Beachy, M. D.; Cao, Y.; Whittington, D. A.; Lippard, S. J.; Friesner, R. A. Large scale ab initio quantum chemical calculation of the intermediates in the soluble methane monooxygenase catalytic cycle. *J. Am. Chem. Soc.* **2000**, *122*, 2828−2839.
(60) Friesner, R. A.; Dunietz, B. D. Large-scale ab initio quantum chemical calculations on biological systems. *Acc. Chem. Res.* **2001**, *34*, 351−358.
(61) Gherman, B. F.; Dunietz, B. D.; Whittington, D. A.; Lippard, S. J.; Friesner, R. A. Activation of the C-H bond of methane by intermediate Q of methane monoozygenase: A theoretical study. *J. Am. Chem. Soc.* **2001**, *123*, 3836−3837.
(62) Baik, M. H.; Lee, D.; Friesner, R. A.; Lippard, S. J. Theoretical studies of diiron(II) complexes that model features of the dioxygen-activating centers in non-heme diiron enzymes. *Isr. J. Chem.* **2001**, *41*, 173−186.
(63) Ambundo, E. A.; Friesner, R. A.; Lippard, S. J. Reactions of methane monooxygenase intermediate Q with derivatized methanes. *J. Am. Chem. Soc.* **2002**, *124*, 8770−8771.
(64) Guallar, V.; Gherman, B. F.; Miller, W. H.; Lippard, S. J.; Friesner, R. A. Dynamics of alkane hydroxylation at the non-heme diiron center in methane monooxygenase. *J. Am. Chem. Soc.* **2002**, *124*, 3377−3384.
(65) Baik, M.-H.; Gherman, B. F.; Friesner, R. A.; Lippard, S. J. Hydroxylation of methane by non-heme diiron enzymes: molecular orbital analysis of C- H bond activation by reactive intermediate Q. *J. Am. Chem. Soc.* **2002**, *124*, 14608−14615.
(66) Guallar, V.; Gherman, B. F.; Lippard, S. J.; Friesner, R. A. Quantum chemical studies of methane monooxygenase: comparision with P450. *Curr. Opin. Chem. Biol.* **2002**, *6*, 236−242.
(67) Gherman, B. F.; Lippard, S. J.; Friesner, R. A. Substrate hydroxylation in methane monooxygenase: quantitative modeling via mixed quantum mechanics/molecular mechanics techniques. *J. Am. Chem. Soc.* **2005**, *127*, 1025−1037.
(68) Torrent, M.; Musaev, D. G.; Morokuma, K.; Basch, H. A density functional study of possible intermediates of the reaction of dioxygen molecule with nonheme iron complexes. 2. "Water-assisted" model studies. *J. Phys. Chem. B* **2001**, *105*, 4453−4463.
(69) Yoshizawa, K. Theoretical study on kinetic isotope effects in the C-H bond activation of alkanes by iron-oxo complexes. *Coord. Chem. Rev.* **2002**, *226*, 251−259.
(70) Hasnain, S. S. *Synchrotron Radiation in Chemistry and Biology II*; Springer: 1988; pp 73−93.
(71) Rosenzweig, A. C.; Brandstetter, H.; Whittington, D. A.; Nordlund, P.; Lippard, S. J.; Frederick, C. A. Crystal structures of the methane monooxygenase hydroxylase from Methylococcus capsulatus (Bath): Implications for substrate gating and component interactions. *Proteins: Struct., Funct., Genet.* **1997**, *29*, 141−152.
(72) Sazinsky, M. H.; Merkx, M.; Cadieux, E.; Tang, S.; Lippard, S. J. Preparation and X-ray Structures of Metal-Free, Dicobalt and Dimanganese Forms of Soluble Methane Monooxygenase Hydroxylase from Methylococcus capsulatus (Bath). *Biochemistry* **2004**, *43*, 16263−16276.
(73) Whittington, D. A.; Lippard, S. J. Crystal structures of the soluble methane monooxygenase hydroxylase from Methylococcus capsulatus (Bath) demonstrating geometrical variability at the dinuclear iron active site. *J. Am. Chem. Soc.* **2001**, *123*, 827−838.

https://doi.org/10.1021/jacs.1c01180
J. Am. Chem. Soc. 2021, 143, 6560−6577

(74) Sazinsky, M. H.; Lippard, S. J. Product Bound Structures of the Soluble Methane Monooxygenase Hydroxylase from Methylococcus capsulatus (Bath): Protein Motion in the α-Subunit. *J. Am. Chem. Soc.* **2005**, *127*, 5814−5825.
(75) Srinivas, V.; Banerjee, R.; Lebrette, H.; Jones, J. C.; Aurelius, O.; Kim, I.-S.; Pham, C. C.; Gul, S.; Sutherlin, K. D.; Bhowmick, A. High-Resolution XFEL Structure of the Soluble Methane Monooxygenase Hydroxylase Complex with its Regulatory Component at Ambient Temperature in Two Oxidation States. *J. Am. Chem. Soc.* **2020**, *142*, 14249−14266.
(76) Jackson Rudd, D.; Sazinsky, M. H.; Merkx, M.; Lippard, S. J.; Hedman, B.; Hodgson, K. O. Determination by X-ray Absorption Spectroscopy of the Fe- Fe Separation in the Oxidized Form of the Hydroxylase of Methane Monooxygenase Alone and in the Presence of MMOD. *Inorg. Chem.* **2004**, *43*, 4579−4589.
(77) Shu, L.; Liu, Y.; Lipscomb, J. D.; Que, L., Jr. X-ray absorption spectroscopic studies of the methane monooxygenase hydroxylase component from Methylosinus trichosporium OB3b. *JBIC, J. Biol. Inorg. Chem.* **1996**, *1*, 297−304.
(78) Vanommeslaeghe, K.; Hatcher, E.; Acharya, C.; Kundu, S.; Zhong, S.; Shim, J.; Darian, E.; Guvench, O.; Lopes, P.; Vorobyov, I. CHARMM general force field: A force field for drug-like molecules compatible with the CHARMM all-atom additive biological force fields. *J. Comput. Chem.* **2010**, *31*, 671−690.
(79) Neese, F. The ORCA program system. *Wiley Interdiscip. Rev.: Comput. Mol. Sci.* **2012**, *2*, 73−78.
(80) Neese, F.; Wennmohs, F.; Becker, U.; Riplinger, C. The ORCA quantum chemistry program package. *J. Chem. Phys.* **2020**, *152*, 224108.
(81) Nelson, M. T.; Humphrey, W.; Gursoy, A.; Dalke, A.; Kalé, L. V.; Skeel, R. D.; Schulten, K. NAMD: a parallel, object-oriented molecular dynamics program. *International Journal of High Performance Computing Applications* **1996**, *10*, 251−268.
(82) Phillips, J. C.; Braun, R.; Wang, W.; Gumbart, J.; Tajkhorshid, E.; Villa, E.; Chipot, C.; Skeel, R. D.; Kale, L.; Schulten, K. Scalable molecular dynamics with NAMD. *J. Comput. Chem.* **2005**, *26*, 1781−1802.
(83) Melo, M. C.; Bernardi, R. C.; Rudack, T.; Scheurer, M.; Riplinger, C.; Phillips, J. C.; Maia, J. D.; Rocha, G. B.; Ribeiro, J. V.; Stone, J. E. NAMD goes quantum: an integrative suite for hybrid simulations. *Nat. Methods* **2018**, *15*, 351.
(84) Becke, A. D. Density-functional exchange energy approximation with correct asymptotic behavior. *Phys. Rev. A: At., Mol., Opt. Phys.* **1988**, *38*, 3098−3100.
(85) Perdew, J. P. Density-Functional Approximation for the Correlation-Energy of the Inhomogeneous Electron-Gas. *Phys. Rev. B: Condens. Matter Mater. Phys.* **1986**, *33*, 8822−8824.
(86) Weigend, F.; Ahlrichs, R. Balanced basis sets of split valence, triple zeta valence and quadruple zeta valence quality for H to Rn: Design and assessment of accuracy. *Phys. Chem. Chem. Phys.* **2005**, *7*, 3297−3305.
(87) Grimme, S.; Ehrlich, S.; Goerigk, L. Effect of the Damping Function in Dispersion Corrected Density Functional Theory. *J. Comput. Chem.* **2011**, *32*, 1456−1465.
(88) Römelt, M.; Ye, S.; Neese, F. Calibration of Modern Density Functional Theory Methods for the Prediction of ^{57}Fe Mössbauer Isomer Shifts: Meta-GGA and Double-Hybrid Functionals. *Inorg. Chem.* **2009**, *48*, 784−785.
(89) Becke, A. D. Density-functional thermochemistry 3. The role of exact exchange. *J. Chem. Phys.* **1993**, *98*, 5648−5652.
(90) Lee, C. T.; Yang, W. T.; Parr, R. G. Developmnt of the Colle-Salvetti correlation energy formula into a functional of the electron density. *Phys. Rev. B: Condens. Matter Mater. Phys.* **1988**, *37*, 785−789.
(91) Neese, F. Prediction and interpretation of the 57Fe isomer shift in Mössbauer spectra by density functional theory. *Inorg. Chim. Acta* **2002**, *337*, 181−192.
(92) Bill, E., The mf program, **2014**.
(93) DeBeer George, S.; Petrenko, T.; Neese, F. Time-dependent density functional calculations of ligand K-edge X-ray absorption spectra. *Inorg. Chim. Acta* **2008**, *361*, 965−972.
(94) Neese, F. Prediction of Molecular Properties and Molecular Spectroscopy with Density Functional Theory: From Fundamental Theory to Exchange-Coupling. *Coord. Chem. Rev.* **2009**, *253*, 526−563.
(95) DeBeer George, S.; Petrenko, T.; Neese, F. Prediction of iron K-edge absorption spectra using time-dependent density functional theory. *J. Phys. Chem. A* **2008**, *112*, 12936−12943.
(96) Chandrasekaran, P.; Stieber, S. C. E.; Collins, T. J.; Que, L., Jr.; Neese, F.; DeBeer, S. Prediction of high-valent iron K-edge absorption spectra by time-dependent Density Functional Theory. *Dalton Trans.* **2011**, *40*, 11070−11079.
(97) Han, W. G.; Liu, T.; Lovell, T.; Noodleman, L. DFT calculations of 57Fe Mössbauer isomer shifts and quadrupole splittings for iron complexes in polar dielectric media: applications to methane monooxygenase and ribonucleotide reductase. *J. Comput. Chem.* **2006**, *27*, 1292−1306.
(98) Liu, T.; Lovell, T.; Han, W.-G.; Noodleman, L. DFT Calculations of Isomer Shifts and Quadrupole Splitting Parameters in Synthetic Iron-Oxo Complexes: Applications to Methane Monooxygenase and Ribonucleotide Reductase. *Inorg. Chem.* **2003**, *42*, 5244−5251.
(99) Bjornsson, R.; Neese, F.; DeBeer, S. Revisiting the Mössbauer Isomer Shifts of the FeMoco Cluster of Nitrogenase and the Cofactor Charge. *Inorg. Chem.* **2017**, *56*, 1470−1477.
(100) Fox, B. G.; Hendrich, M. P.; Surerus, K. K.; Andersson, K. K.; Froland, W. A.; Lipscomb, J. D.; Munck, E. Mössbauer, EPR, and ENDOR studies of the hydroxylase and reductase components of methane monooxygenase from Methylosinus trichosporium OB3b. *J. Am. Chem. Soc.* **1993**, *115*, 3688−3701.
(101) Kauffmann, K. E.; Popescu, C. V.; Dong, Y.; Lipscomb, J. D.; Que, L.; Münck, E. Mössbauer evidence for antisymmetric exchange in a diferric synthetic complex and diferric methane monooxygenase. *J. Am. Chem. Soc.* **1998**, *120*, 8739−8746.
(102) Banerjee, R.; Meier, K. K.; Münck, E.; Lipscomb, J. D. Intermediate P* from Soluble Methane Monooxygenase Contains a Diferrous Cluster. *Biochemistry* **2013**, *52*, 4331−4342.
(103) Banerjee, R.; Komor, A. J.; Lipscomb, J. D. *Methods in Enzymology*; Elsevier: 2017; Vol. *596*, pp 239−290.
(104) Neese, F. Definition of corresponding orbitals and the diradical character in broken symmetry DFT calculations on spin coupled systems. *J. Phys. Chem. Solids* **2004**, *65*, 781−785.
(105) Xue, G.; Wang, D.; De Hont, R.; Fiedler, A. T.; Shan, X.; Münck, E.; Que, L. A synthetic precedent for the [FeIV2 (μ-O) 2] diamond core proposed for methane monooxygenase intermediate Q. *Proc. Natl. Acad. Sci. U. S. A.* **2007**, *104*, 20713−20718.
(106) Sinnecker, S.; Slep, L. D.; Bill, E.; Neese, F. Performance of nonrelativistic and quasi-relativistic hybrid DFT for the prediction of electric and magnetic hyperfine parameters in 57Fe Mössbauer spectra. *Inorg. Chem.* **2005**, *44*, 2245−2254.
(107) Berry, J. F.; DeBeer George, S.; Neese, F. Electronic structure and spectroscopy of "superoxidized" iron centers in model systems: theoretical and experimental trends. *Phys. Chem. Chem. Phys.* **2008**, *10*, 4361−4374.
(108) Krewald, V.; Lassalle-Kaiser, B.; Boron, T. T., III; Pollock, C. J.; Kern, J.; Beckwith, M. A.; Yachandra, V. K.; Pecoraro, V. L.; Yano, J.; Neese, F. The protonation states of oxo-bridged MnIV dimers resolved by experimental and computational Mn K pre-edge X-ray absorption spectroscopy. *Inorg. Chem.* **2013**, *52*, 12904−12914.
(109) DeBeer George, S.; Brant, P.; Solomon, E. I. Metal and Ligand K-Edge XAS of Organotitanium Complexes: Metal 4p and 3d Contributions to Pre-edge Intensity and Their Contributions to Bonding. *J. Am. Chem. Soc.* **2005**, *127*, 667−674.
(110) Kurtz, D. M., Jr. Oxo-and hydroxo-bridged diiron complexes: a chemical perspective on a biological unit. *Chem. Rev.* **1990**, *90*, 585−606.

https://doi.org/10.1021/jacs.1c01180
J. Am. Chem. Soc. 2021, 143, 6560−6577

(111) Pestovsky, O.; Stoian, S.; Bominaar, E. L.; Shan, X.; Münck, E.; Que, L., Jr.; Bakac, A. Aqueous Fe(IV)=O: Spectroscopic Identification and Oxo-Group Exchange. *Angew. Chem.* **2005**, *117*, 7031−7034.
(112) Ye, S.; Neese, F. Nonheme oxo-iron(IV) intermediates form an oxyl radical upon approaching the C-H bond activation transition state. *Proc. Natl. Acad. Sci. U. S. A.* **2011**, *108*, 1228−1233.
(113) Mondal, B.; Roy, L.; Neese, F.; Ye, S. High-Valent Iron-Oxo and-Nitrido Complexes: Bonding and Reactivity. *Isr. J. Chem.* **2016**, *56*, 763−772.
(114) Geng, C.; Ye, S.; Neese, F. Analysis of Reaction Channels for Alkane Hydroxylation by Nonheme Iron(IV)-Oxo Complexes. *Angew. Chem., Int. Ed.* **2010**, *49*, 5717−5720.
(115) Solomon, E. I.; Wong, S. D.; Liu, L. V.; Decker, A.; Chow, M. S. Peroxo and oxo intermediates in mononuclear nonheme iron enzymes and related active sites. *Curr. Opin. Chem. Biol.* **2009**, *13*, 99−113.
(116) Denisov, I. G.; Makris, T. M.; Sligar, S. G.; Schlichting, I. Structure and chemistry of cytochrome P450. *Chem. Rev.* **2005**, *105*, 2253−2278.
(117) Lee, S.-K.; Lipscomb, J. D. Oxygen activation catalyzed by methane monooxygenase hydroxylase component: Proton delivery during the O- O bond cleavage steps. *Biochemistry* **1999**, *38*, 4423−4432.
(118) Liu, K. E.; Valentine, A. M.; Wang, D.; Huynh, B. H.; Edmondson, D. E.; Salifoglou, A.; Lippard, S. J. Kinetic and spectroscopic characterization of intermediates and component interactions in reactions of methane monooxygenase from Methylococcus capsulatus (Bath). *J. Am. Chem. Soc.* **1995**, *117*, 10174−10185.
(119) Tinberg, C. E.; Lippard, S. J. Revisiting the mechanism of dioxygen activation in soluble methane monooxygenase from M. capsulatus (Bath): evidence for a multi-step, proton-dependent reaction pathway. *Biochemistry* **2009**, *48*, 12145−12158.
(120) Valentine, A. M.; Stahl, S. S.; Lippard, S. J. Mechanistic studies of the reaction of reduced methane monooxygenase hydroxylase with dioxygen and substrates. *J. Am. Chem. Soc.* **1999**, *121*, 3876−3887.
(121) Nesheim, J. C.; Lipscomb, J. D. Large kinetic isotope effects in methane oxidation catalyzed by methane monooxygenase: Evidence for C-H bond cleavage in a reaction cycle intermediate. *Biochemistry* **1996**, *35*, 10240−10247.
(122) Liu, A.; Jin, Y.; Zhang, J.; Brazeau, B. J.; Lipscomb, J. D. Substrate radical intermediates in soluble methane monooxygenase. *Biochem. Biophys. Res. Commun.* **2005**, *338*, 254−261.
(123) Deighton, N.; Podmore, I. D.; Symons, M. C.; Wilkins, P. C.; Dalton, H. Substrate radical intermediates are involved in the soluble methane monooxygenase catalysed oxidations of methane, methanol and acetonitrile. *J. Chem. Soc., Chem. Commun.* **1991**, 1086−1088.
(124) Jin, Y.; Lipscomb, J. D. Probing the Mechanism of C- H Activation: Oxidation of Methylcubane by Soluble Methane Monooxygenase from Methylosinus trichosporium OB3b. *Biochemistry* **1999**, *38*, 6178−6186.
(125) Brazeau, B. J.; Austin, R. N.; Tarr, C.; Groves, J. T.; Lipscomb, J. D. Intermediate Q from soluble methane monooxygenase hydroxylates the mechanistic substrate probe norcarane: evidence for a stepwise reaction. *J. Am. Chem. Soc.* **2001**, *123*, 11831−11837.
(126) Dalton, H.; Wilkins, P.; Deighton, N.; Podmore, I.; Symons, M. Electron paramagnetic resonance studies of the mechanism of substrate oxidation by methane monooxygenase. *Faraday Discuss.* **1992**, *93*, 163−171.
(127) Choi, S.-Y.; Eaton, P. E.; Kopp, D. A.; Lippard, S. J.; Newcomb, M.; Shen, R. Cationic species can be produced in soluble methane monooxygenase-catalyzed hydroxylation reactions; radical intermediates are not formed. *J. Am. Chem. Soc.* **1999**, *121*, 12198−12199.
(128) Wilkins, P. C.; Dalton, H.; Podmore, I. D.; Deighton, N.; Symons, M. C. Biological methane activation involves the intermediacy of carbon-centered radicals. *Eur. J. Biochem.* **1992**, *210*, 67−72.
(129) Liu, K. E.; Johnson, C. C.; Newcomb, M.; Lippard, S. J. Radical clock substrate probes and kinetic isotope effect studies of the hydroxylation of hydrocarbons by methane monooxygenase. *J. Am. Chem. Soc.* **1993**, *115*, 939−947.
(130) Valentine, A. M.; LeTadic-Biadatti, M.-H.; Toy, P. H.; Newcomb, M.; Lippard, S. J. Oxidation of ultrafast radical clock substrate probes by the soluble methane monooxygenase from Methylococcus capsulatus (Bath). *J. Biol. Chem.* **1999**, *274*, 10771−10776.
(131) Baik, M.-H.; Newcomb, M.; Friesner, R. A.; Lippard, S. J. Mechanistic studies on the hydroxylation of methane by methane monooxygenase. *Chem. Rev.* **2003**, *103*, 2385−2420.
(132) Ansari, M.; Senthilnathan, D.; Rajaraman, G. Deciphering the origin of million-fold reactivity observed for the open core diiron $[HO\text{-}Fe^{III}\text{-}O\text{-}Fe^{IV}{=}O]^{2+}$ species towards C-H bond activation: role of spin-states, spin-coupling, and spin-cooperation. *Chem. Sci.* **2020**, *11*, 10669−10687.

https://doi.org/10.1021/jacs.1c01180
J. Am. Chem. Soc. 2021, 143, 6560−6577